



## Stability of jets and wakes confined by compliant walls

Ryan Poole  and M. R. Turner *School of Mathematics and Physics, University of Surrey, Guildford GU2 7XH, United Kingdom*

(Received 29 November 2022; accepted 16 May 2023; published 5 June 2023)

A spatiotemporal stability analysis is conducted on a flow representing both jets and wakes, subject to confinement by identical compliant walls. The walls are placed at equal distances from the fluid center line for a range of wall and flow parameters. By following the position of special saddle points (pinch points) of the dispersion relation in the complex wave-number plane, the absolute and convective instability stability properties of the flow are determined for various system parameters. The compliant walls are shown to modify the shear-induced instabilities, which exist in the rigid wall case, as well as introduce new additional instabilities originating from the presence of the wall itself. It is observed that under certain system parameters, these wall-induced modes become the dominant instability present in the system and can induce an absolute instability into flows which are only convectively unstable when confined by rigid walls, as well as extending the region of absolute instability to large confinement parameters. Results are presented for both a piecewise linear velocity profile and a smooth velocity profile, with the results of the two studies in qualitative agreement.

DOI: [10.1103/PhysRevFluids.8.063901](https://doi.org/10.1103/PhysRevFluids.8.063901)

### I. INTRODUCTION

This study is concerned with the stability of two-dimensional (2D) jets and wakes. These 2D jet or wake flows consist of a central fluid, sandwiched between two identical fluids, all of which are infinite in the streamwise direction, and bounded above and below by two walls. See Fig. 1 for a schematic diagram of the flow. When the velocity of the inner fluid is greater than that of the outer fluid, i.e.,  $U_1 > U_2$ , we have a jet, while when  $U_1 < U_2$  we have a wake.

The stability of both jets and wakes has been extensively studied in the literature. Huerre and Monkewitz [1] examined two simplified versions of these flows, namely a bluff body wake and a symmetric planar jet. It was found that for the case of the bluff body, there is a region of absolute instability (AI) in the immediate wake, which leads to an unstable global shear mode downstream, which ultimately leads to vortex shedding. This AI region thus makes the flow act as a self-excited oscillator. Regions of AI were also found in the low density jet, which again led to a global instability. Hence identifying regions of AI and understanding how to control them is a significant area of interest. One such example is in controlling the turbulence behind air- or seacraft as a result of their wakes. This has the potential of reducing drag on these vehicles, improving their efficiency, as well as reducing fluid turbulence in the region. This is a particular issue for seacraft, as human-made noise has been known to impact a number of oceanic ecosystems [2].

The transition from convective instability (CI) to AI is due to the interaction between the two shear layers and not due to viscosity [3]. Thus approximating the fluids as inviscid fluids captures

---

*Published by the American Physical Society under the terms of the [Creative Commons Attribution 4.0 International](https://creativecommons.org/licenses/by/4.0/) license. Further distribution of this work must maintain attribution to the author(s) and the published article's title, journal citation, and DOI.*

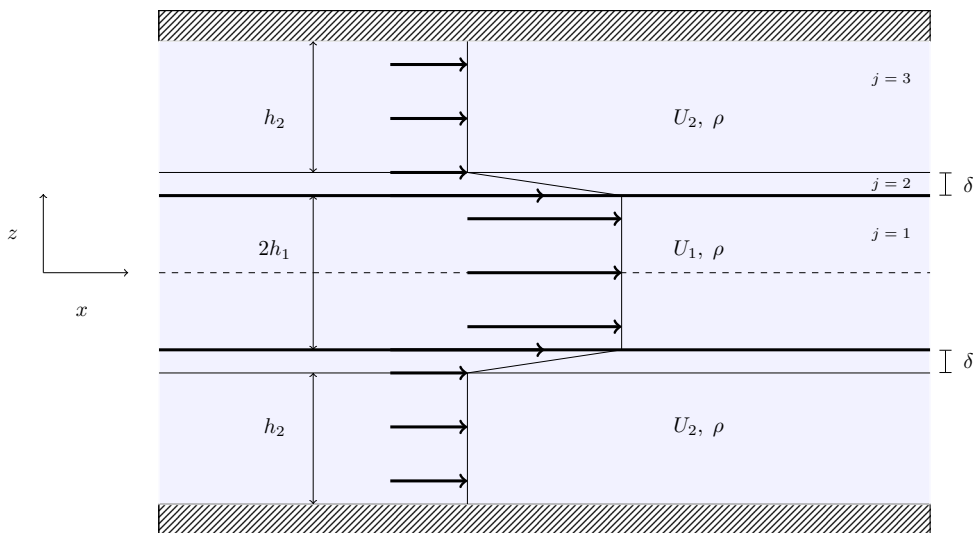


FIG. 1. Schematic of the plug flow velocity profile with shear layers, which is considered in this paper. Both fluids have density  $\rho$ . The inner fluid has velocity  $U_1 \hat{x}$  and width  $2h_1$ , while the outer fluid has velocity  $U_2 \hat{x}$  and width  $h_2 + \delta$ , where  $\delta$  is the shear layer width. Fluid interfaces are represented by thick black lines at  $z = \pm h_1$ .

the key significant stability properties. Yu and Monkewitz [3] also investigated the density ratio of the two fluids, identifying low-density jets and high-density wakes as needing lower shear rates to invoke an AI.

Juniper and Candel [4] used the simple flow setup in Fig. 1 to investigate the consequence of confining the jet or wake flow between two rigid walls in order to explain an AI seen in coaxial injectors. Juniper [5] then extended this study to thoroughly investigate the effect of confinement by rigid walls on jets and wakes. He discovered that unstable modes of zero group velocity exist in the unconfined jet or wake flow, and these are enhanced by the addition of rigid walls. This is due to the fact that the addition of the walls aids in the constructive interference between modes whose wavelength scales with the thickness of the inner and outer layers, respectively. This was further extended to take into account the full impulse response, in particular showing that transverse propagating convective instabilities can set up absolute instabilities in confined flows [6,7], as well as the AI of swirling jets [8].

In the current paper we investigate the linear response of the jet or wake flow in Fig. 1 when we replace the rigid bounding walls with two identical compliant, or flexible, walls, a schematic for which is given in Fig. 2. The inclusion of these compliant walls is expected to allow for the control these instabilities, either making them more unstable or more stable. This added control has many practical applications, from noise damping to reducing drag.

The type of compliant wall we consider in Fig. 2 is a ‘‘Kramer’’-type compliant wall and were initially designed to model dolphin skin [9]. The wall itself is modelled as a spring backed elastic plate with a viscous fluid behind the plate acting as a damping substrate. Such a boundary can be easily realized mathematically and as such it has been used as a compliant wall model for flows such as channel flows and flows above a compliant rotating disk [10–15]. In these flows the compliant boundary leads to a rich variety of instabilities, including instabilities which originate due to the flexibility of the boundary.

The layout of the current paper is as follows: In Sec. II, we derive the governing equations for the flow pictured in Fig. 1, as well as suitable boundary conditions at the compliant walls. Dispersion relations are derived for both varicose and sinuous modes for both finite shear layer thicknesses

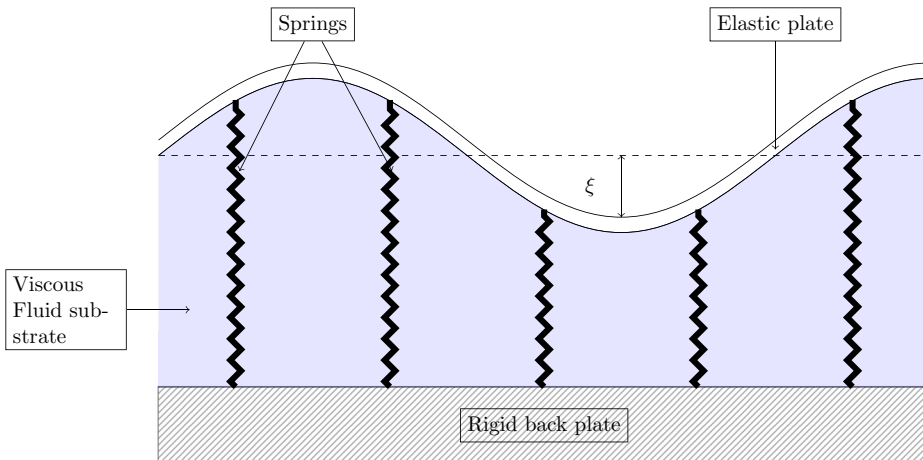


FIG. 2. A diagram of the spring-backed elastic plate compliant wall model considered here. The springs all share the same spring constant, and  $\xi$  is the displacement of the elastic sheet from the undisturbed position represented by the dashed line.

$\delta$  and in the plug flow limit  $\delta \rightarrow 0$ . In Sec. III we present a temporal stability analysis of the compliant wall dispersion relation, in particular highlighting the new wall-induced modes which exist. In Sec. IV we discuss the spatiotemporal analysis used to identify the AI growth rates from special saddle points in the complex wave-number plane and present results of the spatiotemporal analysis for a range of flow and wall parameters. In the results we highlight the effect of the various wall parameters on the piecewise linear velocity profile and a smooth velocity profile and show that the presence of a compliant wall can induce an absolute instability, particularly in weakly confined flows, where the rigid wall case is only convectively unstable. We discuss the implication of including viscosity in Sec. V with conclusions and remarks given in Sec. VI.

## II. FLOW SETUP AND GOVERNING EQUATIONS

We consider the two-dimensional flow setup as shown in Fig. 1 consisting of three inviscid fluid regions bounded above and below. We consider a homogeneous setup with each fluid region having density  $\rho$ . The outer two fluids have width  $h_2$  and constant horizontal velocity  $U_2 \hat{\mathbf{x}}$ , while the inner flow has half width  $h_1$  and constant horizontal velocity  $U_1 \hat{\mathbf{x}}$ . Here  $(x, z)$  are Cartesian coordinates with corresponding unit vectors  $\hat{\mathbf{x}}$  and  $\hat{\mathbf{z}}$ , respectively. While we assume both fluids are inviscid for stability purposes, we consider the velocities of the two fluids to be continuously connected by a linear shear layer of constant thickness  $\delta$  in the outer fluid. The flow is bounded above and below by two compliant walls, and we assume the parameters governing the physical properties of these walls are identical, this allows us to take advantage of the symmetry of the flow. Hence, we limit our attention to the upper half of the flow with the origin of  $z$  axis at the center of the inner flow. We make the assumption at the outset that the walls are only permitted to move in the  $z$  direction, so that the upper wall is located at  $z_{\text{wall}} = h_1 + h_2 + \delta + \xi(x, t)$ , where  $\xi(x, t)$  is the wall-normal displacement from the wall's equilibrium position.

We define the upper half of the base flow  $\underline{u} = U(z) \hat{\mathbf{x}}$  as the piecewise linear flow,

$$U(z) = \begin{cases} U^{(3)} = U_2, & h_1 + \delta \leq z \leq h_1 + h_2 + \delta \\ U^{(2)} = (U_2 - U_1) \frac{(z - h_1 - \delta)}{\delta} + U_2, & h_1 \leq z \leq h_1 + \delta \\ U^{(1)} = U_1, & 0 \leq z \leq h_1. \end{cases} \quad (1)$$

It has been shown that the qualitative stability properties of flows of the form (1) are largely unaffected by the piecewise linear form of the shear velocity profile at leading order when compared to smooth profiles, and hence we choose to use it here in order to construct analytical dispersion relations for the instability waves [3]. We also note that we have neglected the addition of boundary layers at the walls of the domain, an assumption which is valid, assuming that their contribution to the growth of disturbances is small. This turns out to be a valid assumption at moderate and weak confinements, but as we will discuss, this assumption may not hold at stronger confinements. A more detailed discussion about the influences of boundary layers can be found in Sec. V.

We consider the velocity vector  $\underline{u}^{(j)}(x, z, t) = (u^{(j)}(x, z, t), w^{(j)}(x, z, t))$  for  $j = 1, 2, 3$ , where the layers are numbered from the middle layer outward (see Fig. 1), which satisfy the Euler equations,

$$\frac{\partial \underline{u}^{(j)}}{\partial t} + \underline{u}^{(j)} \cdot \nabla \underline{u}^{(j)} = -\frac{1}{\rho} \nabla p^{(j)}, \quad (2)$$

$$\nabla \cdot \underline{u}^{(j)} = 0, \quad (3)$$

where  $p^{(j)}(x, z, t)$  is the pressure. In (2), we have neglected gravitational effects as we assume the flow velocities are large and hence gravity is not a main driver for the instability. At  $z = z_{\text{wall}}$  the flow has to satisfy the governing compliant wall boundary condition, which states that the normal pressure force of the fluid must balance the normal acceleration at the wall, i.e.,

$$p^{(3)}(x, h_1 + h_2 + \delta + \xi(x, t), t) = \hat{\mathbf{n}} \cdot \hat{\mathbf{a}}, \quad (4)$$

where  $\hat{\mathbf{n}}$  is the unit normal to the wall and  $\hat{\mathbf{a}}$  is the acceleration vector. In Sec. II A we are ultimately interested in linear perturbations of the wall, hence the only component of  $\hat{\mathbf{a}}$  we consider is the  $\hat{\mathbf{z}}$  component, which we model as a spring backed elastic plate, with equation

$$\hat{\mathbf{a}} \cdot \hat{\mathbf{z}} = \left( m \frac{\partial^2}{\partial t^2} + d \frac{\partial}{\partial t} + B \frac{\partial^4}{\partial x^4} - T \frac{\partial^2}{\partial x^2} + K_E \right) \xi(x, t).$$

Here  $m = \rho_e b$  the mass per unit area of the wall, where  $\rho_e$  is the density of the elastic plate and  $b$  is the plate thickness. We also have  $d$  the damping coefficient and  $B$  the flexural rigidity of the wall, which describes the force couple required to bend the wall. The longitudinal tension of the plate,  $T$ , measures the tension per unit length, while  $K_E = K - g(\rho - \rho_s)$  is the ‘‘adjusted’’ spring stiffness,<sup>1</sup> where  $\rho_s$  is the density of the wall substrate and  $K$  is the spring stiffness. The fluid pressure in the outer fluid is given by  $p^{(3)}$ .

At the wall the fluid must also satisfy the kinematic boundary condition. Which due to the assumption of wall motion only in the  $z$  direction, takes the form

$$\frac{\partial \xi}{\partial t} + u^{(3)} \frac{\partial \xi}{\partial x} = w^{(3)}, \quad (5)$$

at  $z = h_1 + h_2 + \delta + \xi(x, t)$ .

### A. Linearization of problem

To study the stability properties of this flow, we examine small flow and wall displacements with a time periodic frequency  $\omega$  and spatial wave number  $\alpha$ . Namely, we write

$$\begin{aligned} \underline{u}^{(j)}(x, z, t) &= U^{(j)}(z) \hat{\mathbf{x}} + \epsilon (\hat{u}^{(j)}(z), \hat{w}^{(j)}(z)) \exp[i(\alpha x - \omega t)] + \text{c.c.}, \\ p(x, z, t) &= P^{(j)} + \epsilon \hat{p}^{(j)}(z) \exp[i(\alpha x - \omega t)] + \text{c.c.}, \end{aligned} \quad (6)$$

<sup>1</sup>Note that in the rest of this work, we will replace  $K_E$  with just  $K$ .

and

$$\xi(x, t) = \epsilon \widehat{\xi} \exp[i(\alpha x - \omega t)] + \text{c.c.}, \quad (7)$$

where  $0 < \epsilon \ll 1$  such that we can linearize (2)–(5). Here  $U^{(j)}$  is the component of (1) in each layer respectively,  $P^{(j)}$  are constant pressures in each layer,  $\widehat{\xi}$  is a constant, and c.c. denotes complex conjugate.

By substituting (6) into (2), we find that the linear equations at order  $O(\epsilon)$  for the flow perturbation quantities are

$$-i\omega \widehat{u}^{(j)} + i\alpha U^{(j)} \widehat{u}^{(j)} + \widehat{w}^{(j)} D U^{(j)} = -\frac{i\alpha}{\rho} \widehat{p}^{(j)}, \quad (8)$$

$$-i\omega \widehat{w}^{(j)} + iU \alpha \widehat{w}^{(j)} = -\frac{1}{\rho} D \widehat{p}^{(j)}, \quad (9)$$

$$i\alpha \widehat{u}^{(j)} + D \widehat{w}^{(j)} = 0, \quad (10)$$

where  $D \equiv d/dz$ .

Similarly, we linearize (4) and (5) about small wall-normal perturbations by substituting in (7) and retaining terms of order  $O(\epsilon)$  only. Thus (5) becomes

$$-i\omega \widehat{\xi} + U_2 i\alpha \widehat{\xi} = \widehat{w}^{(3)}, \quad (11)$$

now evaluated at the equilibrium position  $z = h_1 + h_2 + \delta$ , while (4) becomes

$$(-m\omega^2 - i\omega d + B\alpha^4 + T\alpha^2 + K)\widehat{\xi} = \widehat{p}^{(3)}, \quad (12)$$

again evaluated at  $z = h_1 + h_2 + \delta$ . Note that  $O(\epsilon^2)$  terms have been neglected from the right hand side of (11) which arise from the linearization about  $|\xi| \ll 1$ .

### B. Dispersion relation

Given the linearized equations (8)–(12), we can now derive the dispersion relation for this flow. First, we eliminate  $\widehat{p}^{(j)}$  and  $\widehat{u}^{(j)}$  from (8) using (9) and (10). This leads us to the Rayleigh equation for the normal velocity perturbation  $\widehat{w}^{(j)}$ ,

$$(\alpha U - \omega)(D^2 - \alpha^2)\widehat{w}^{(j)} - \alpha D^2 U^{(j)} \widehat{w}^{(j)} = 0. \quad (13)$$

Since our base flow (1) is piecewise linear, then  $D^2 U^{(j)} = 0$  in each layer, thus (13) reduces to  $(D^2 - \alpha^2)\widehat{w}^{(j)} = 0$ , with solutions in each layer written as

$$\widehat{w}^{(3)} = A_3 e^{\alpha(z-h_1-\delta)} + B_3 e^{-\alpha(z-h_1-\delta)}, \quad (14)$$

$$\widehat{w}^{(2)} = A_2 \cosh[\alpha(z-h_1)] + B_2 \sinh[\alpha(z-h_1)], \quad (15)$$

$$\widehat{w}^{(1)} = A_1 \cosh(\alpha z) + B_1 \sinh(\alpha z). \quad (16)$$

Given the symmetry of the flow about the line  $z = 0$ , there are two types of modes we need to consider, varicose modes (which have an antisymmetric vertical velocity about  $z = 0$ ) with  $A_1 = 0$ , and sinuous modes (which have a symmetric vertical velocity about  $z = 0$ ) with  $B_1 = 0$ .

At the interfaces of the different base profile regions, namely at  $z = h_1$  and  $z = h_1 + \delta$ , we require that both the perturbation pressure and the displacement of the fluid interface are continuous, which leads to the jump conditions

$$\Delta \left[ \frac{\widehat{w}^{(j)}}{\alpha U^{(j)} - \omega} \right] = 0, \quad \text{and} \quad \Delta [\rho(\alpha U^{(j)} - \omega) D \widehat{w}^{(j)} - \alpha \rho D U^{(j)} \widehat{w}^{(j)}] = 0, \quad (17)$$

respectively, where  $\Delta = \lim_{\zeta \rightarrow 0} [\cdot]_{z_n - \zeta}^{z_n + \zeta}$  and  $z_n$  is the equilibrium interface position [16].

Satisfying these jump conditions and eliminating all coefficients except  $A_3, B_3$ , allows us to express the relationship between the spatial wave number  $\alpha$  and the temporal frequency  $\omega$  in form

of the dispersion relation

$$\mathbb{D}^{(v,s)}(\alpha, \omega) \equiv A_3 D_+^{(v,s)} + B_3 D_-^{(v,s)} = 0. \quad (18)$$

Here the superscript  $v$  and  $s$  denote the varicose and sinuous dispersion relations, respectively, and

$$D_{\mp}^v \equiv [V_1 \alpha \delta \coth(\alpha h_1) + 1] \{V_2 \alpha \delta [\cosh(\alpha \delta) \pm \sinh(\alpha \delta)] - \sinh(\alpha \delta)\} \\ \pm V_1 \alpha \delta \{V_2 \alpha \delta [\cosh(\alpha \delta) \pm \sinh(\alpha \delta)] \mp \cosh(\alpha \delta)\}, \quad (19)$$

with

$$V_k = \frac{U_k - c}{U_2 - U_1}, \quad k = 1, 2, \quad \text{and} \quad c = \frac{\omega}{\alpha}. \quad (20)$$

Note that for the sinuous modes in (18),  $D_{\pm}^s$  are defined exactly as (19), except with  $\coth(\alpha h_1)$  replaced with  $\tanh(\alpha h_1)$ .

To complete the derivation of the dispersion relations, we must derive a second equation connecting  $A_3$  and  $B_3$ , which comes from considering the compliant wall boundary condition. Using (11) together with (8)–(10), we can write the boundary condition (12) as

$$Q \widehat{w}^{(3)} = \frac{\rho}{\alpha^2} (\alpha U_2 - \omega)^2 D \widehat{w}^{(3)}, \quad (21)$$

at  $z = h_1 + h_2 + \delta$  where we define  $Q(\alpha, \omega) = (-m\omega^2 - i\omega d + B\alpha^4 + T\alpha^2 + K)$ . This quantity is related to the wall impedance term used to model acoustic wall linings [17]. Substituting in the expression for  $\widehat{w}^{(3)}$  from (14), we can write this in the compact form

$$\frac{A_3}{B_3} = -e^{-2\alpha h_2} \left[ \frac{Q + \alpha \rho (U_2 - c)^2}{Q - \alpha \rho (U_2 - c)^2} \right], \quad (22)$$

where in the limit as  $Q \rightarrow \infty$ , the wall becomes rigid and we obtain the boundary condition for a rigid wall bounded flow [6]. For more details on how to derive dispersion relations for piecewise linear flow profiles the reader is referred to Ref. [18] or Ref. [16].

To reduce the number of free parameters in the problem, we choose to nondimensionalize by setting  $h_1$  as our characteristic length scale,  $U_{\text{ref}} = (U_1 + U_2)/2$  as our characteristic velocity scale and  $\rho$  as our characteristic density scale. Hence, we define the shear parameter  $\Lambda = (U_1 - U_2)/(U_2 + U_1)$ . When  $|\Lambda| > 1$ , we experience counter flow, where the inner and outer fluids move in opposite directions. When  $|\Lambda| < 1$  we experience coflow, where both fluids are moving in the same direction. Finally, when  $|\Lambda| = 1$ , one of either the two flows, depending on whether we have a jet or a wake, is stationary compared to the second flow. We define the shear layer thickness  $\delta = \delta^* h_1$  and confinement ratio  $h = h_2/h_1$ , along with the wall parameters

$$m = \rho h_1 m^*, \quad d = \rho U_{\text{ref}} d^*, \quad B = \rho h_1^3 U_{\text{ref}}^2 B^*, \quad T = \rho h_1 U_{\text{ref}}^2 T^*, \\ K = \frac{\rho U_{\text{ref}}^2}{h_1} K^*, \quad Q = \frac{\rho U_{\text{ref}}^2}{h_1} Q^*, \quad \alpha = \alpha^*/h_1, \quad \omega = \omega^* U_{\text{ref}}/h_1, \quad (23)$$

where the stars denote nondimensionalized quantities. Thus, using (22), we then obtain the following compliant wall dispersion relations:

$$\mathbb{D}^{(v,s)*}(\alpha, \omega) \equiv \alpha Q [-e^{-2\alpha h} D_+^{(v,s)*} + D_-^{(v,s)*}] \\ + (\alpha(1 - \Lambda) - \omega)^2 [-e^{-2\alpha h} D_+^{(v,s)*} - D_-^{(v,s)*}] = 0, \quad (24)$$

and  $D_{\pm}^{(v,s)*}$  and  $D_{\pm}^{(v,s)}$  are the nondimensional forms of (19), given by

$$D_{\mp}^{v*} \equiv [V_1^* \alpha^* \delta^* \coth(\alpha^*) + 1] \{V_2^* \alpha^* \delta^* [\cosh(\alpha^* \delta^*) \pm \sinh(\alpha^* \delta^*)] - \sinh(\alpha^* \delta^*)\} \\ \pm V_1^* \alpha^* \delta^* \{V_2^* \alpha^* \delta^* [\cosh(\alpha^* \delta^*) \pm \sinh(\alpha^* \delta^*)] \mp \cosh(\alpha^* \delta^*)\}. \quad (25)$$

Here

$$V_j^* = -\frac{(1 \pm \Lambda) - c^*}{2\Lambda} \quad \text{and} \quad c^* = \frac{\omega^*}{\alpha}, \quad (26)$$

where  $V_1$  contains the  $1 + \Lambda$  term, while  $V_2$  contains the  $1 - \Lambda$  term. Again, sinuous versions of these expressions are obtained by replacing  $\coth(\alpha^*)$  with  $\tanh(\alpha^*)$ .

We can consider the form of the dispersion relations in the limit  $\delta \rightarrow 0$  by taking a Taylor expansion of (25) for  $\alpha\delta \ll 1$ . In this limit the leading order,  $O(\alpha\delta)$ , terms cancel out, while the  $O[(\alpha\delta)^2]$  terms, when rearranged, give the dispersion relations for the plug flow profile in the  $\delta \rightarrow 0$  limit of the form

$$\mathbb{D}^{(v,s)*}(\alpha^*, \omega^*) = \alpha^* Q^* X^{(v,s)*} - [\alpha^*(1 - \Lambda) - \omega^*]^2 Y^{(v,s)*} = 0. \quad (27)$$

Where for varicose modes we have

$$\begin{aligned} X^{v*} &= [\alpha^*(1 - \Lambda) - \omega^*]^2 \coth(\alpha^* h) + [\alpha^*(1 + \Lambda) - \omega^*]^2 \coth(\alpha^*), \\ Y^{v*} &= [\alpha^*(1 - \Lambda) - \omega^*]^2 + [\alpha^*(1 + \Lambda) - \omega^*]^2 \coth(\alpha^*) \coth(\alpha^* h), \end{aligned} \quad (28)$$

and for sinuous modes we replace the  $\coth(\alpha^*)$  terms with  $\tanh(\alpha^*)$ . Again, taking  $Q \rightarrow \infty$  recovers the plug flow dispersion relations for the rigid wall case [5], given by  $\mathbb{D}^{(v,s)*} = X^{(v,s)*} = 0$ .

In Ref. [5] (i.e., in the  $Q \rightarrow \infty$  limit) it was shown that for  $\delta = 0$  there exists the transformation  $(\text{var}, \Lambda, h) \longleftrightarrow (\text{sin}, -\Lambda, h)$  which links the properties of varicose and sinuous modes. We observe similar useful transformations in the  $\delta = 0$  case, which are  $(\text{var}, \Lambda, h, Q = 0) \longleftrightarrow (\text{sin}, -\Lambda, h, Q = \infty)$  and  $(\text{sin}, \Lambda, h, Q = 0) \longleftrightarrow (\text{var}, -\Lambda, h, Q = \infty)$ . Namely, a sinuous mode in the rigid wall limit ( $Q = \infty$ ) has the same dispersion relation as a varicose mode in the  $Q \rightarrow 0$  limit and vice versa, where  $Q \rightarrow 0$  corresponds to having a fluid-air interface at  $z = h_1 + h_2 + \delta$ , i.e.,  $p^{(3)} = 0$ . This transformation gives us information about the stability properties of the flow at the two extreme ends of the wall parameter magnitudes.

In the remainder of the paper we consider only the nondimensional dispersion relations and we drop the stars from our notation with the understanding that the variables are dimensionless.

### III. TEMPORAL INSTABILITY ANALYSIS

In this section, we consider the effects of compliant walls on the temporal instability of sinuous modes in jet or wake flows (varicose modes behave in a qualitatively similar way, and so we do not discuss these here). The dispersion relations, both with  $\delta = 0$  and  $\delta \neq 0$ , are fourth-order polynomials in  $\omega$  with transcendental coefficients in  $\alpha$ . In the rigid wall limit, the dispersion relation reduces to a second-order polynomial, hence the compliant walls introduce two new modes. The temporal analysis is conducted by numerically calculate roots of the sinuous dispersion relation (27) at each real  $\alpha$  using the standard root finding function, `root`, in MATLAB. The roots are arranged in order of descending  $c_i (= \omega_i/\alpha)$ , and we plot those modes for  $c_i \geq 0$ . Any mode with  $c_i = 0$  is neutrally stable, whereas any mode with  $c_i > 0$  is considered temporally unstable and values of  $c_i < 0$  are considered temporally stable. Note, for walls with no damping ( $d = 0$ ) the polynomials have real coefficients, hence the values of  $c$  are either real, or appear in complex conjugate pairs. When wall damping is included then the polynomial coefficients become complex and so this restriction on the forms of  $c$  no longer hold.

In Fig. 3 we plot  $c_i(\alpha)$  for the temporally growing modes for three wall configurations, and for  $\Lambda = 3, h = 1.5$  in the limit  $\delta \rightarrow 0$ . We compare these results to the rigid wall case to better understand the behavior of the two additional modes of instability which are introduced with the compliant walls. In each panel the dominant mode for a given  $\alpha$  is represented in red, whereas the subdominant mode is plotted in green. For the parameters considered here we only observe two unstable modes at any one value of  $\alpha$ .

In the rigid wall limit in Fig. 3(a), we only have two modes (complex conjugates) with only one mode exhibiting  $c_i \geq 0$ . For nonrigid walls in Figs. 3(b)–3(d), we find that the behavior of

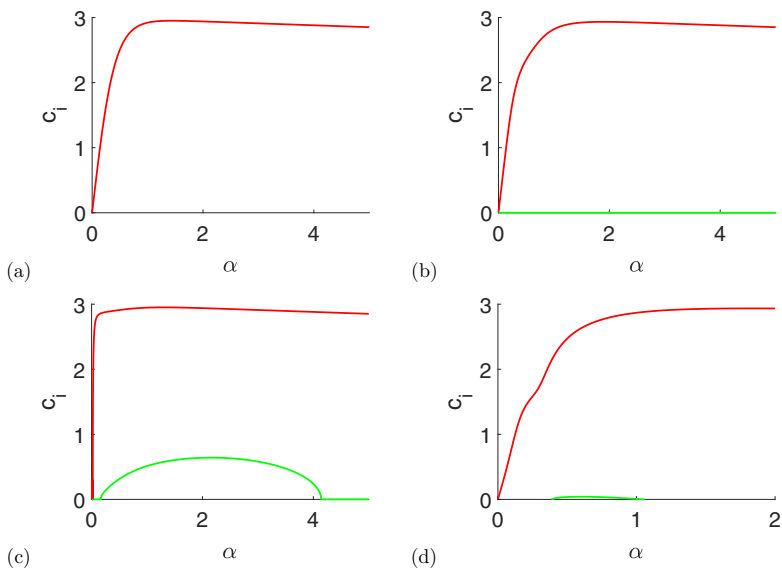


FIG. 3. Plots of  $c_i(\alpha)$  for four different wall configurations: (a) rigid wall, (b)  $(B, T, K, m, d) = (2, 0, 10, 0.1, 0)$ , (c)  $(B, T, K, m, d) = (0.015, 0.025, 0.01, 0.1, 0)$ , and (d)  $(B, T, K, m, d) = (1, 1.5, 1.5, 0.1, 0.55)$ . The red line signifies the dominant shear-induced mode, while the green line gives the subdominant wall-induced mode.

the dominant mode (red) varies when compared to the rigid wall case, i.e., we do not converge to the maximum  $c_i \approx \Lambda = 3$  at the same rate as the rigid wall case for example, but we also have a second mode which could also become unstable. In Fig. 3(b) the modes due to the presence of the wall are neutrally stable, while Fig. 3(c) is an example of the wall generating a second (complex conjugate pair) unstable mode. In this latter case the *wall-induced* mode (green line) is unstable for  $\alpha \approx [0.16, 4.14]$  but remains subdominant to the *shear-induced* mode (red line) which exists in the rigid-wall limit. In Fig. 3(d) we consider a wall with damping ( $d \neq 0$ ) and so in this case the modes are not complex conjugates. Here we see just the two unstable modes, but again the wall-induced mode has a much smaller growth rate than the shear-induced mode.

To understand why we term these modes wall-induced and shear-induced modes, we consider the forms of the pressure eigenmodes in Fig. 4 for the four cases in Fig. 3. The pressure eigenmode, in nondimensional form, is found via (8) and (10) as

$$\widehat{p}^{(j)}(z) = -\frac{i}{\alpha^2}[\alpha(1 \pm \Lambda) - \omega]D\widehat{w}^{(j)}, \quad (29)$$

where because we have considered  $\delta = 0$ , we can set  $DU^{(j)} \equiv 0$ . In each case we term the shear-induced mode [which exists in the rigid-wall limit in Fig. 4(a)] as the one which attains its global pressure maximum at the shear layer, while the wall-induced mode attains its global pressure maximum at the wall ( $z = 2.5$ ).

This brief temporal stability study shows that while the wall-induced modes typically have a temporal growth rate which is less than the shear-induced modes, they could become significant to the global stability of the flow when the evolution of wave packets (superposition of all possible waves) and their absolute instability is considered in the next section.



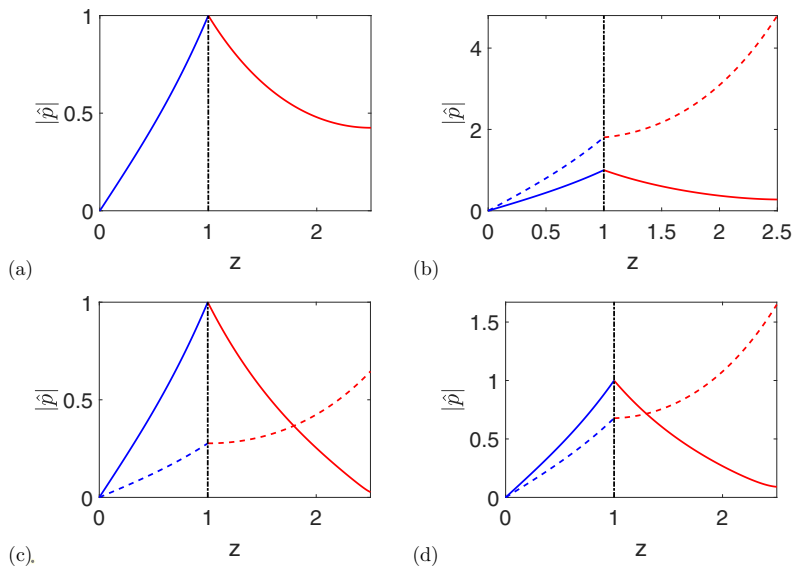


FIG. 4. Plots of the absolute values of sinuous pressure eigenmodes  $|\widehat{p}|$  as a function of  $z$  for the wall configurations given in Fig. 3. Here we fix  $\Lambda = 3$ ,  $h = 1.5$ , and  $\alpha = 1$  and normalized such that  $|\widehat{p}| = 1$  at  $z = 1$  for the mode represented with the solid lines. Solid lines represent the dominant shear-induced mode while dashed lines represent the subdominant wall-induced mode. The vertical black dashed-dot line represents the fluid interface at  $z = 1$ .

#### IV. ABSOLUTE INSTABILITY ANALYSIS

In this section, our focus is on the AI characteristics of the flow, and hence we undertake a spatiotemporal stability analysis where we consider both  $\alpha, \omega \in \mathbb{C}$ . This spatiotemporal analysis, considers growth of wave packets, rather than individual waves, in both space and time simultaneously. If these wave packets grow both upstream and downstream of the point at which the instability is generated, then this constitutes an absolute instability, and because the base flow is parallel, this also constitutes a global instability. If we only observe growth downstream of the initial impulse, and decay in time, then this constitutes a CI.

We identify AIs by considering the vertical velocity perturbation response, given by

$$w(x, z, t) = \frac{1}{4\pi^2} \int_F \int_L \frac{\widehat{w}(z)}{\mathbb{D}(\alpha, \omega)} e^{i(\alpha x - \omega t)} d\alpha d\omega, \quad (30)$$

where the inversion contours  $F, L$  lie in the complex  $\alpha$  and  $\omega$  planes, respectively. To carry out the integration in the  $\omega$  plane, we require the  $L$  contour to lie above all singularities in the  $\omega$  plane, i.e., at some constant  $\omega_i > 0$ , spanning from  $-\infty$  to  $\infty$  in the  $\omega_r$  direction for  $\omega = \omega_r + i\omega_i$ . Note that if we have no flow stabilizing mechanism, such as viscosity, then surface tension or shear layers of finite thickness between the inner and outer flows, then we have an infinite number of singularities with increasingly large  $\omega_i$ . This can be seen in Fig. 5, which highlights the effect of reducing  $\delta$  on  $\omega_i$  for the temporal instability with  $\alpha \in \mathbb{R}$ .

Having infinitely many singularities where  $\omega_i$  is arbitrarily large means we cannot place the  $L$  contour above them all, resulting in an ill-posed problem [17]. However, if we were to assume the existence of a small stabilizing mechanism, and let this tend to zero, then this means there will be a maximum singularity, albeit one with very large, but finite,  $\omega_i$ , above which we can place  $L$ .

The response  $w(x, z, t)$  is associated with a forcing term [19]. We consider a forcing which is localized at the shear layer, so as to excite all modes equally at  $(x, t) = (0, 0)$ . Juniper [6] shows

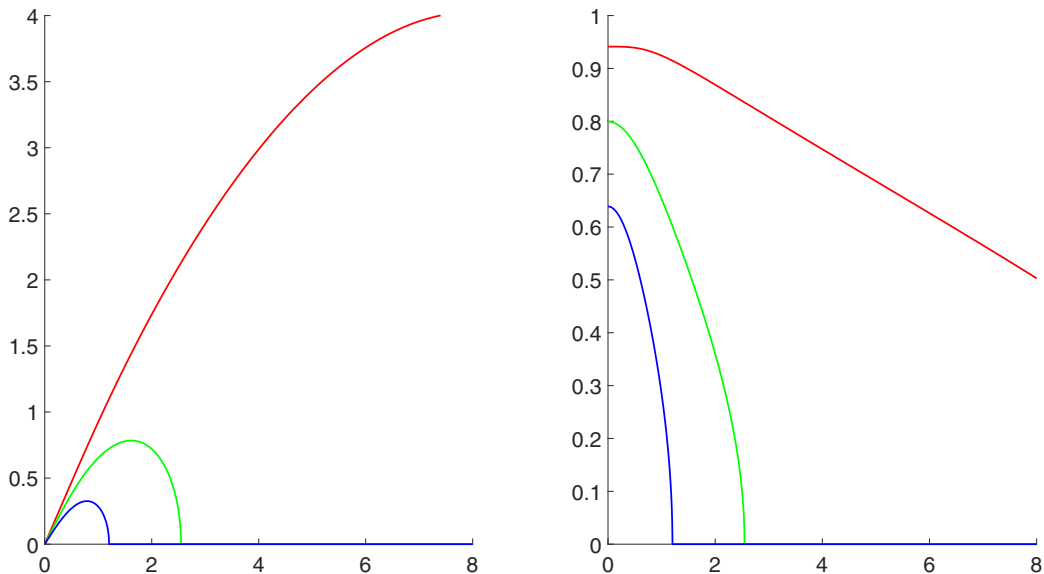


FIG. 5. The plot on the left shows rigid wall ( $Q \rightarrow \infty$ ) temporal instability growth rate  $\omega_i$  as a function of  $\alpha$  for varicose modes for  $\delta = 1$  (blue line),  $\delta = 0.5$  (green line), and  $\delta = 0.1$  (red line). The right plot is the equivalent phase velocity  $c_i = \omega_i/\alpha$ . Here  $\Lambda = 1$  and  $h = 1.5$ . This result is for the rigid wall case, and hence the two values of  $\omega$  are either real or complex conjugate pairs.

that the physical structure of the forcing in the  $z$  direction does not affect the response (30), just so long as it is isolated in  $x$  and  $t$  at the shear layer  $z = h_1$ . It is possible to consider the response (30) away from the shear layer, the so-called *full response*, but this is not considered here [6,7].

Evaluating the Laplace integral using Residue calculus gives

$$w(x, z, t) = \frac{1}{2\pi} \sum_m \int_F \frac{\widehat{w}(z) e^{-i(\omega_m(\alpha) - \alpha \frac{x}{\tau})t}}{\mathbb{D}_\omega(\alpha, \omega_m)} d\alpha, \quad (31)$$

which is to be evaluated by integrating along the contour  $F$  which we initially take to lie on the real  $\alpha$  axis in the complex  $\alpha$  plane. Here we are summing over  $m$  singularities in the  $\omega$  plane, and the  $\omega$  subscript denotes partial differentiation with respect to  $\omega$ . The form of  $\mathbb{D}_\omega$  for (24) is given in the Appendix. Since the path of the integration contour is arbitrary, we could keep  $F$  on the real  $\alpha$  axis and still get a solution for (31). However, to infer information about the large  $t$  behavior of the flow, we adopt the method of steepest descent, which deforms  $F$  through the valleys of points in the  $\alpha$  plane with zero group velocity, i.e., saddle points that satisfy  $\mathbb{D}^{(v,s)}(\alpha, \omega) = \mathbb{D}_\alpha^{(v,s)}(\alpha, \omega) = 0$ , where the  $\alpha$  subscript denotes partial differentiation with respect to  $\alpha$  [7,20]. These saddles are referred to as pinch points, but it is important to note that not every saddle in the  $\alpha$  plane corresponds to a pinch point. The form of  $\mathbb{D}_\alpha$  for (24) is given in the Appendix.

To identify whether a saddle point is a pinch point, we either do this by eye, in unambiguous cases, by observing that the inversion contour  $F$  can be deformed such that it lies solely in the valleys of  $\omega_i$  contours [7], or we use Briggs' criterion [21] which examines whether the hill of the saddle consists of downstream and upstream propagating branches. However, in those ambiguous cases, we can consider the growth rate of the AI by evaluating (31) numerically using high-precision calculations. To evaluate (31) first we calculate values of  $\omega_i \geq 0$  for each mode for values along the  $\alpha_r$  axis to high precision, making use of the arbitrary precision package of Smith [22]. This is essentially a temporal instability calculation as seen in Figs. 3 and 5. We require high precision in this calculation as the numerical evaluation of the integral in (31) requires adding and subtracting

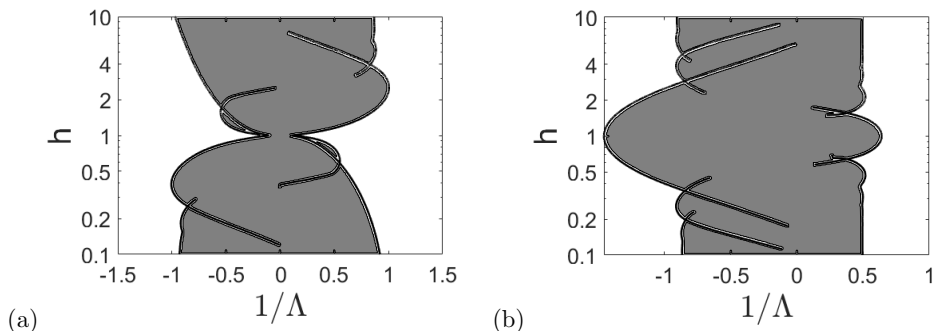


FIG. 6. Regions of AI (gray) in  $(\frac{1}{\Lambda}, h)$  space for (a) varicose modes and (b) sinuous modes in the rigid wall limit where  $\delta \rightarrow 0$ . White regions represent regions of CI.

exponentially large terms. Therefore to avoid numerical errors from building up and contaminating the solution, we calculate the form of  $\omega_m(\alpha)$  to 300 significant figures. We then integrate (31) along the real  $\alpha$  axis with  $x/t = 0$  using the trapezoidal rule. Then the numerical growth rate is given by

$$\omega^{\text{num}} = \frac{iw_t(0, h_1, t)}{w(0, h_1, t)}, \quad (32)$$

where the subscript  $t$  represents partial differentiation with respect to time. In the limit  $t \rightarrow \infty$  the numerical value of (32) gives the same value of  $\omega$  at the dominate saddle point.

To present results for the AI properties of the flow we consider numerical solutions of the dispersion relations (25) and (27). We use Newton's method to simultaneously solve  $\mathbb{D}(\alpha, \omega) = \mathbb{D}_\alpha(\alpha, \omega) = 0$  iteratively, and this is documented in the Appendix. Initial guesses for  $(\alpha^0, \omega^0)$  at the saddle points are found by plotting contours of constant  $\omega_i$  in the complex  $\alpha$  plane, such as in Fig. 7. These initial guesses are then iterated on until the distance between successive iterations is less than  $10^{-8}$ . We then adjust one of the flow or wall parameters by a small amount and use the calculated value as an initial guess for this parameter set.

### A. Absolute instability destabilization and control via compliant walls

In this section, we discuss the effect of varying wall parameters on the absolute instability of the flow for a selection of wall parameters. By allowing the walls to be compliant, additional modes of instability are introduced, as discussed in Sec. III, which we term wall-induced modes. These

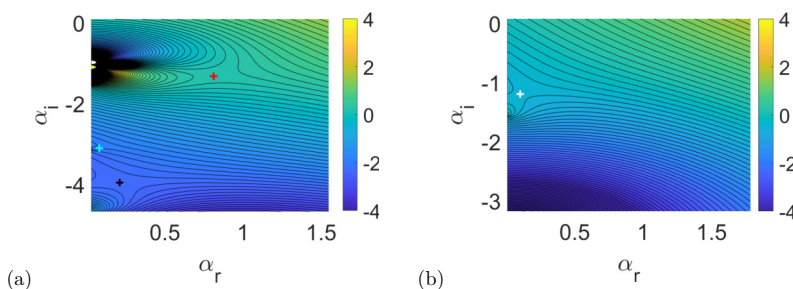


FIG. 7. Plot of  $\omega_i$  contours in the  $\alpha$  plane for the varicose mode in the (a)  $Q \rightarrow 0$  limit and (b)  $Q \rightarrow \infty$  limit for  $(\Lambda, h) = (1, 0.5)$ , which corresponds to case 2. In (a) we define saddle 1 (red cross), saddle 2 (cyan cross), and saddle 3 (black cross), where only saddles 1 and 2 are pinch points, while in (b) the dominant saddle is given by the white cross.

modes, and how they affect the systems instability will be discussed in more detail in the next section when we discuss the effects of confinement on the flows stability.

In the rigid wall limit, the regions of  $(\Lambda, h; \delta)$  parameter space for which an AI exists has been mapped out by Juniper [5] in the limit as  $\delta \rightarrow 0$ , and have been recreated in Figs. 6(a) and 6(b), for varicose and sinuous modes, respectively. The gray regions represent regions of AI, while the white regions represent regions of CI. These regions are found using a numerical scheme which follows the contour  $\omega_i = 0$  as documented in the Appendix of Ref. [23].

These regions show that both varicose and sinuous modes can maintain AIs even in the unconfined ( $h \rightarrow \infty$ ) limit, and the growth rates of these AI modes grow larger as  $|\Lambda|$  increases. This is a result of us moving into a region of counterflow, where fluid in the inner and outer layers of the flow move in opposite directions, meaning that we obtain a stronger Kelvin-Helmholtz instability at the fluid interface  $z = h_1$ .

In this paper we do not attempt to remap these  $\delta = 0$  AI regions of parameter space for all wall parameters as the effect of varying these parameters is quantitatively similar for multiple parameters. Instead, we highlight a few examples specifically focusing close to the AI-CI transition boundary from Fig. 6, i.e., weakly absolutely unstable flows, showing how the AI can be enhanced or controlled in the presence of compliant walls.

It is of interest to identify cases where flow properties change from AI to CI, or vice versa, as we vary a given wall parameter to show the destabilization or control on the instability induced by the wall compliance. By using the transform noted at the end of Sec. II, in the  $\delta \rightarrow 0$  limit, it was observed that the varicose mode dispersion relation in the  $Q \rightarrow 0$  limit is the same dispersion relation as for a sinuous mode in the rigid wall limit, under the transform  $\Lambda \rightarrow -\Lambda$  and vice versa. Note that this does not mean that a varicose mode in the  $Q \rightarrow 0$  limit becomes a sinuous mode in the  $Q \rightarrow \infty$  limit, just that its dispersion relation is the same as for sinuous modes. When identifying saddle points by solving  $\mathbb{D}^v(\alpha, \omega) = \mathbb{D}_\alpha^v(\alpha, \omega) = 0$ , all these modes are varicose modes for all wall and flow parameter values. The same is true for sinuous modes when using  $\mathbb{D}^s$  to replace  $\mathbb{D}^v$ . Using the above dispersion relation observation means that by choosing suitable parameters our flow can sit within one of the four cases:

- (1) Case 1: an AI as  $Q \rightarrow 0$  and an AI as  $Q \rightarrow \infty$ ,
- (2) Case 2: an AI as  $Q \rightarrow 0$  and a CI or stability as  $Q \rightarrow \infty$ ,
- (3) Case 3: a CI or stability as  $Q \rightarrow 0$  and an AI as  $Q \rightarrow \infty$ ,
- (4) Case 4: a CI or stability as  $Q \rightarrow 0$  and a CI or stability as  $Q \rightarrow \infty$ .

This suggests that compliant walls can stabilize a flow compared to the rigid wall limit, as in case 3, or destabilize the flow compared to the rigid wall limit, as seen in in case 2. Cases 1 and 4 are not discussed in detail here, as we only wish to focus on the stabilizing or destabilizing properties of compliant walls rather than their effect of maintaining a consistent instability behavior.

By using the above transformation and comparing Figs. 6(a) and 6(b), we are able to identify combinations of  $(\Lambda, h)$  which produce the four cases stated above. The majority of the parameter pairs correspond to cases 1 and 4 for both varicose and sinuous modes in the rigid wall limit. However, there are parameters where the AI regions under this transformation do not overlap perfectly, in particular around  $h = 1$ . These regions generate case 2 and 3 flows. Since we are interested in the change of stability properties due to the effect of the walls, we focus only one example of case 2 and one example of case 3.

As we noted in the previous section, the  $Q \rightarrow 0$  limit corresponds to having a fluid-air interface at the flow boundary, and physically, this limit is difficult to reach for an experimentally realized wall, as the wall mass  $m$  typically cannot be zero. However, we find that the four cases noted above are also realizable if we consider the limit of  $Q$  becoming small but nonzero. Hence we can investigate the effect of each wall parameter on the AI of the flow separately by setting all but one of the wall parameters to zero and then varying this parameter from near zero to a large value, effectively taking the rigid wall limit. While this approach is difficult to realize physically, as materials cannot have their parameters individually tuned in this way, mathematically we are able to investigate their effect in this way. First, we consider a case 2 varicose mode with  $(\Lambda, h) = (1, 0.5)$ , which corresponds

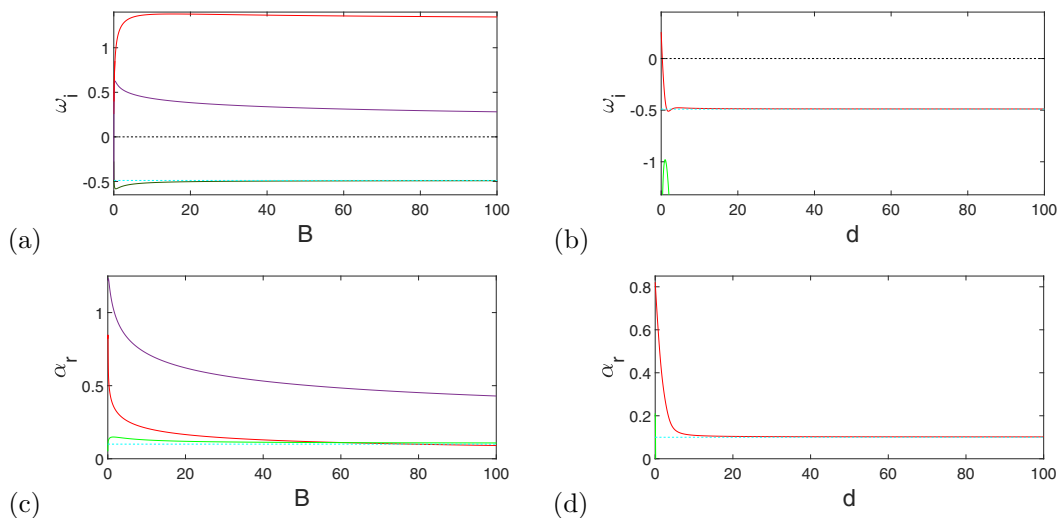


FIG. 8. Case 2: Plot of the varicose AI growth rates  $\omega_i$  of saddle 1 (red), as we vary (a) flexural rigidity  $B$  and (b) the damping coefficient  $d$ . Dashed lines represent growth rates in the rigid wall limit. Note the existence of two new modes in (a) represented by green and purple curves. Panels (c) and (d) represents the evolution of the wave number  $\alpha_r$  for each mode as we vary  $B$  and  $d$ , respectively.

to a jet where the outer flow is stationary, at strong confinement. In Fig. 7(a) we plot contours of constant  $\omega_i$  in the  $\alpha$  plane in the  $Q \rightarrow 0$  limit and observe three saddle points, each labeled with a cross. Note that in this limit, the dominant pinch point is saddle 1 (red cross) with  $\omega_i \approx 0.255$ . This is the only pinch point with a positive growth rate. As the wall parameter values are varied from zero, the position and value of  $\omega$  at these saddles varies, and, ultimately, as  $Q \rightarrow \infty$ , the  $\alpha$  plane ends up in the form given in Fig. 7(b). What we are interested in examining in this section is how the transition between the two  $\alpha$  planes occurs, because, as we will show, it is not always the most dominant saddle in Fig. 7(a) which transforms into the most dominate saddle in Fig. 7(b) where  $\omega_i \approx -0.485$ .

In Fig. 8 we examine how the value of  $\omega_i$  at the saddle points identified in Fig. 7. We only consider the AI growth rate variation while varying the parameters  $B$  and  $d$  in this case because similar behaviors are seen when varying the other parameters. The AI growth rates of the varicose mode, as a function of  $B$ , in Fig. 8(a) shows two new modes emerging, shown in purple and dark green, respectively, which become a factor in the flows instability properties as we increase  $B$ . The saddle represented by the dark green curve converges to the required growth rate in the rigid wall limit (lower blue dashed line), while saddle 1 (red curve) remains with  $\omega_i > 0$  in this limit. However, this is not consistent with the flow being convectively unstable in this limit. The resolution to this is that saddle 1 loses its pinch point status to the new purple saddle when the value of  $\omega_i$  becomes equal at both saddles at  $B \approx 0.04$ . This is because the growth rate of the AI needs to be continuous as the parameters are varied, which means that dominance of a mode can only change at a point where the two modes have the same value of  $\omega_i$  ( $\omega_r$  can be discontinuous though) [24].

The interesting phenomena here is we still have a small positive growth rate from the purple saddle result, even for large finite  $B$  values. But  $\omega_i$  for this saddle converges to zero as  $B \rightarrow \infty$ , the rigid wall limit. This mode appears from the negative  $\alpha_r = \text{Re}(\alpha)$  plane on another Riemann sheet and moves towards the origin as  $B$  varies, as shown in Fig. 8(c). This means that, even for larger  $B$ , we have a vanishingly small AI and that AI mode has an increasingly longer wavelength. Such a mode is reminiscent of the so-called divergence modes discovered by Benjamin [10,11] and Carpenter [14]. This is an interesting feature, as this highlights how the compliant walls can enhance

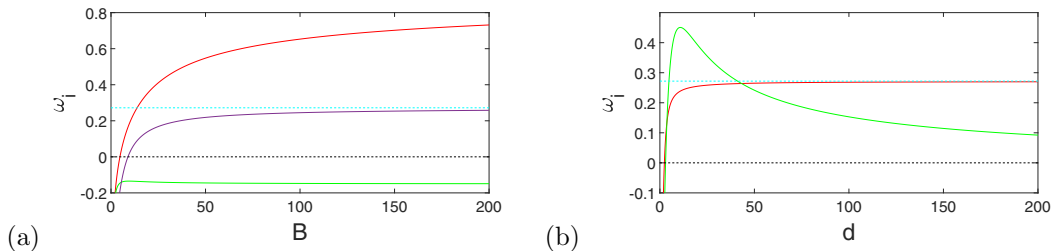


FIG. 9. Case 3: Plot of the sinuous AI growth rates  $\omega_i$  of saddle 1 (red) and saddle 2 (green) as we vary (a) flexural rigidity  $B$  and (b) the damping coefficient  $d$ . Dashed lines represent growth rates in the rigid wall limit. Note that in (a) a new saddle appears, represented by the purple line.

and extend the AI region of existence of a flow with different flow parameters. We also observe this behavior when we vary wall mass  $m$  and longitudinal tension  $T$  (not shown).

Now we consider sinuous modes for a case 3 region of parameter space where  $(\Lambda, h) = (-0.91, 1.10)$ , i.e., where we observe a CI in the  $Q \rightarrow 0$  limit, and AI in the rigid wall limit. Consider Fig. 9, which shows the effects of (a) flexural rigidity  $B$  and (b) the damping coefficient  $d$  on the AI growth rate for the sinuous modes. It is immediately clear from both these figures that the flow very quickly changes from convectively unstable to absolutely unstable as both wall parameters are increased from zero independently. The other three wall parameters, not plotted here, give a similar behavior.

In the case of Fig. 9(a), we observe an AI for  $B > 9.5$  and  $d > 2.1$ . This highlights a small window of parameter space for which we are able to stabilize shear-induced modes. Note that in the case of Fig. 9(a), saddle 1 (red) loses its pinch point status to a new mode (purple) at very small  $B$  values, meaning that, although it has a positive growth rate at large  $B$ , this mode is not a pinch point and hence can be neglected in this discussion. The new mode (purple) then converges to the rigid wall limit growth rate. Furthermore, Fig. 9(b) initially suggests that saddle 2 (green) dominates the flow for  $d \lesssim 45$ ; however, this mode is not a pinch point in this region and can be neglected, leaving saddle 1 (red) to converge to the dominant growth rate in the rigid wall limit.

All the analysis up to this point has been for flows with zero shear layer thickness,  $\delta = 0$ . When  $0 < \delta \ll 1$  a new saddle, labeled  $S_1$  in Ref. [5], exists that cuts off other modes from the inversion contour  $F$  as  $\delta$  increases by limiting the number of unstable modes in the flow. When  $\delta$  is “small,” this saddle exists at  $\alpha_r$  large, and hence this mode has a short wavelength which [6] argues will quickly saturate when nonlinear terms are included, and thus the main flow contribution to the AI or CI nature of the flow is from the saddles we have already considered. Assuming this to be also the case here, we find that the inclusion of finite  $\delta$  leads to qualitatively similar results to those presented in this section, except typically with reduced growth rate values,  $\omega_i$ .

To summarize, the inclusion of compliant walls can have a stabilizing or destabilizing effect on global instabilities in jets and wakes. In particular, the greatest variation in growth rates appears to occur for small wall parameters, i.e., for light flexible walls. We have also shown that wall-induced modes can become a factor in the system’s instability in the form of divergence modes.

Next we will consider a more realistic example of a compliant wall with multiple nonzero parameters and show how varying the confinement ratio  $h$  leads to changes in the AI response.

### B. Effect of confinement with compliant walls on AI

In this section we consider how confinement effects the effectiveness of compliant walls in destabilizing or stabilizing modes of AI. Similarly to the previous section, we follow pinch points in the  $\alpha$  plane while varying the confinement parameter  $h$ . In this analysis, we consider a specific wall with parameters  $K = 10$ ,  $m = 0.1$ , and  $T = d = 0$  held fixed, and we consider various values of  $B = 0.1, 1, 2$ . By having multiple wall parameters nonzero we now have a more realistic problem

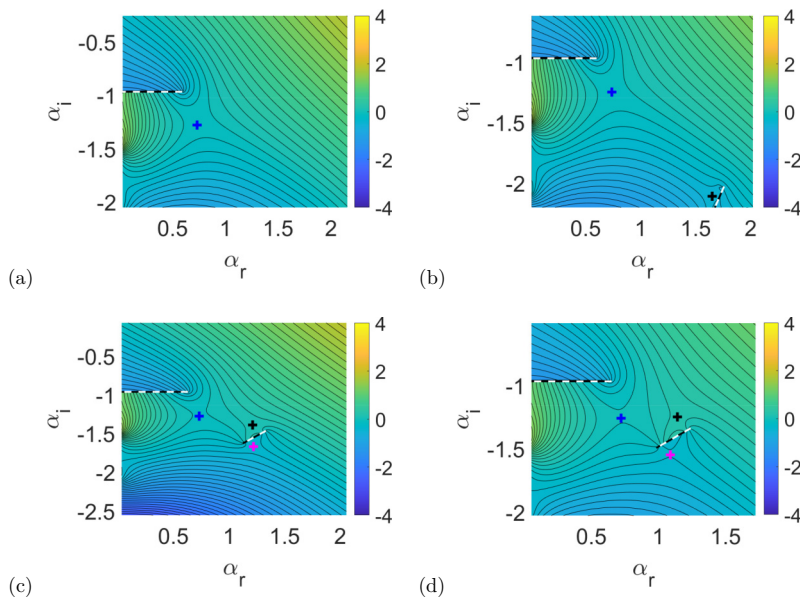


FIG. 10. Contours of constant  $\omega_i$  in the  $\alpha$  plane as we vary the flexural rigidity  $B$  for a varicose mode with parameters  $(\Lambda, h) = (1, 1.5)$  and  $(m, K, d, T) = (0.1, 10, 0, 0)$ . Here (a)  $B = 0$ , (b)  $B = 0.1$ , (c)  $B = 0.5$ , and (d)  $B = 0.75$ , and the black and magenta marked saddles are wall-induced modes and are a consequence of having the compliant walls, while the blue cross represents the location of the flow or wall-enhanced mode  $WI_1$ . The black and white dashed lines represent branch cuts.

to what was considered in the previous section. This also allows us to see how different wall characteristics interact with each other, further destabilizing or stabilizing the flow.

First, we consider a varicose mode with  $\Lambda = 1$ . As before we focus initially on the case  $\delta = 0$ , but we will need to consider  $\delta \neq 0$  in order to evaluate (32) numerically, when we wish to identify the AI growth rate as the saddle points in the complex  $\alpha$  plane become ambiguous. In the rigid wall limit, this parameter setup only experiences a marginal unstable AI mode at  $h \approx 2.38$  [5]. The question we hope to answer is, in general how is this instability affected by the introduction of compliant walls? In Fig. 10 we consider how the complex  $\alpha$  plane for this varicose mode is modified as we increase the flexural rigidity of the wall from  $B = 0$  to  $B = 0.75$ . At  $B = 0$  in Fig. 10(a) we see a single shear-induced mode, which we refer to as  $SI_1$ , marked with a blue cross, and there is also a branch cut which joins the branch point at  $\alpha = 0.5959 - 0.9613i$  to another branch point in  $\alpha_r < 0$ . These branch cuts are not evident in the  $Q \rightarrow 0$  or  $Q \rightarrow \infty$  limits in Fig. 7, and in these limits there are a series of branch cuts all situated down the imaginary axis [5]. There is no one wall parameter which induces these new branch points to exist and are just a consequence of the complex form of the compliant boundary condition. Having additional branch cuts in the complex wave-number plane is not a problem per se, but, as we will see, their existence can make determining whether saddle points are also pinch points and more challenging. The position of the branch points can be found by solving  $\mathbb{D}^{(v)}(\alpha, \omega) = \mathbb{D}_\omega^{(v)}(\alpha, \omega) = 0$  numerically. As we increase  $B$  from zero in Figs. 10(b), 10(c), and 10(d) we observe two additional saddle points moving towards the positive  $\alpha_r$  axis. The modes, represented by these black and magenta crossed saddle points, are wall-induced modes as introduced in Sec. III. These are referred to as  $WI_1$  and  $WI_2$  saddles, respectively

As  $B$  is increased, the two wall-induced mode saddles move through the  $\alpha$  plane and the respective value of  $\omega_i$  at these saddles increases, and it soon becomes unclear whether or not the wall-induced modes end up becoming pinch points and hence the dominant AI mode. This is because the position of the Fourier inversion contour, as it is modified off the real  $\alpha$  axis, is masked

by the branch cuts. To try and understand the AI nature of the flow in this case, we consider the value of  $\omega_i$  at each of these saddle points for  $B = 0.1$  (red), 1 (green), and 2 (blue) in Fig. 11.

Noting again that the AI growth rate needs to be a continuous function of  $h$ , it is clear for  $B = 2$  that there are possibilities for a change in dominance around  $h \approx 1.5, 2.5, 2.8,$  and  $5.8$  depending on which modes are pinch points. Here the solid lines represent the  $SI_1$  shear-induced mode, the wall-induced mode  $WI_2$  is represented by dotted line (note, this saddle only appears in the  $B = 2$  case), while the dashed lines represent the  $WI_1$  wall-induced mode. The black curve represents the rigid wall limit. Due to the branch cuts, and hence multiple interacting Riemann sheets, determining which saddle points lie on the inverse Fourier contour, and hence are pinch points, by eye becomes difficult and ambiguous. Also, using the Briggs criteria calculation becomes cumbersome due to the complexity of the  $\alpha$  plane, where the Briggs contours need to be tracked over multiple Riemann sheets.

To overcome this issue and identify the AI growth rate for this problem we use the numerical evaluation of (31), namely  $\omega^{\text{num}}$  from (32). As we are unable to perform this integral for  $\delta = 0$ , we consider  $\delta \neq 0$  and then consider the result as  $\delta \rightarrow 0$ . Note that we need to choose  $\delta$  sufficiently large such that the integration converges along the contour yet small enough so that the corresponding shear layer saddle,  $S_1$ , highlighted in Ref. [5], does not dominate the flow. As it happens,  $\delta$  need not be very large for this approach to give accurate results in this case.

In this figure we find that varying  $B$  destabilizes the system in much the same way as the varicose mode case, namely we find that the shear-induced mode  $SI_1$  (given in the rigid wall case as the solid black line) is subdominant to the two wall-induced modes,  $WI_1$  and  $WI_2$ , represented by the dashed and dotted curves, respectively. We again see that these modes appear at their most unstable at strong confinement and can sustain an AI even at weak confinement, but Fig. 12 clarifies that we have found all dominant pinch points using the same approach as in Fig. 13 for the varicose modes. As for the varicose mode, the wavelength of the WI modes is typically shorter than the SI mode, but again, this wavelength increases as  $B$  increases.

One feature of the results in both Fig. 11 for the varicose case and Fig. 14 for the sinuous case is that the inclusion of compliant walls can introduce an AI response to the flow (where there was not one in the rigid wall limit), which exists even when the walls are placed far from the central jet or wake. We can make some predictions as to when we expect this to be the case, or when we can expect the flow to have no AI, by considering the dispersion relation as  $h \rightarrow \infty$ . Specifically, we consider the varicose mode, which for  $\delta = 0$  with  $h \rightarrow \infty$  (27) leads to

$$\mathbb{D}^{(v)} = [\alpha Q - (\alpha(1 - \Lambda) - \omega)^2][(\alpha(1 - \Lambda) - \omega)^2 + S(\alpha(1 + \Lambda) - \omega)^2 \coth(\alpha)] = 0. \quad (33)$$

The left square bracket corresponds to the wall-induced modes, while the right square bracket corresponds to the shear-induced modes. The behavior seen at large  $h$  in Figs. 11 and 14 occurs when the two modes have equal frequencies. This corresponds to a solution where

$$\alpha Q - [\alpha(1 - \Lambda) - \omega]^2 = [\alpha(1 - \Lambda) - \omega]^2 + S[\alpha(1 + \Lambda) - \omega]^2 \coth(\alpha) = 0, \quad (34)$$

which can be combined into a single equation of  $\alpha$  or this pair of equations can be solved simultaneously.

In Fig. 15 we plot  $\omega_i$  and the corresponding  $\alpha_r$  value for the case when (34) is satisfied as a function of  $B$  for the varicose and sinuous modes problems from Figs. 11 and 14. For the varicose mode in Fig. 15(a) and 15(b) we see that the AI as  $h \rightarrow \infty$  for  $1 \lesssim B \lesssim 29$  with a maximum growth rate of  $\omega_i \approx 0.105$ , while in Fig. 15(c) and 15(d) the sinuous mode has an AI in this case for  $0 \lesssim B \lesssim 75$  and, unlike the varicose mode, has a maximum value as  $B \rightarrow 0$ . The corresponding  $\alpha_r$  plots show that the wavelengths of the modes seem to converge to  $\alpha_r \approx 0.5$  as  $B$  increases. As the



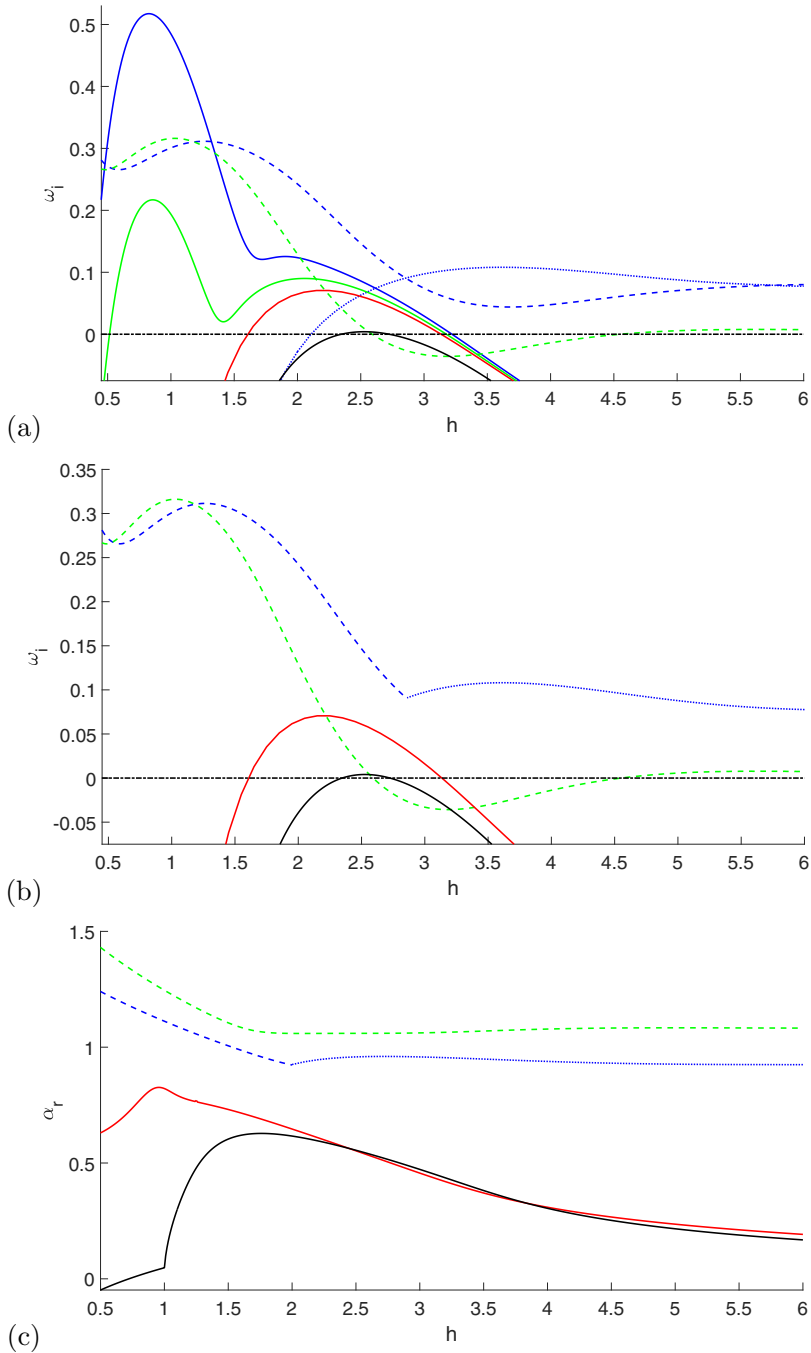


FIG. 11. (a) Plot of the growth rate  $\omega_i$  of the three saddle points in Fig. 10 as a function of the confinement parameter  $h$ . The other fixed parameters are  $(\Lambda, S) = (1, 1)$  with wall parameters  $K = 10$ ,  $m = 0.1$ ,  $T = d = 0$ , and  $B = 0.1$  (red line),  $B = 1$  (green lines), and  $B = 2$  (blue lines). The rigid wall limit result is given by the black line. The dashed lines represent the growth rates of the new  $WI_1$  saddle found by adding compliant walls, while the dotted line (only for  $B = 2$ ) represents the  $WI_2$  wall mode. Plot (b) shows the dominant growth rate curves only, maintaining the line style to highlight which mode takes dominance, while (c) gives the values of  $\alpha_r$  for these dominate modes.

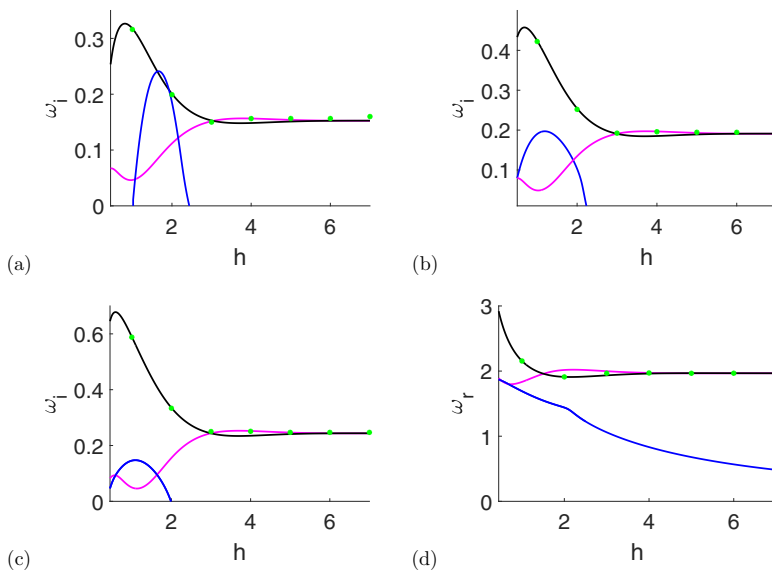


FIG. 12. Sinuous mode: Plots of AI growth rate  $\omega_r$  as a function of confinement  $h$  as we vary shear layer thickness (a)  $\delta = 0.5$ , (b)  $\delta = 0.35$ , and (c)  $\delta = 0.15$ , where the dots represent  $\omega_r^{\text{num}}$  values. The other flow parameters are as in Fig. 14 with  $B = 2$ . In panel (d) we plot  $\omega_r$  for the case  $\delta = 0.15$ , corresponding to panel (c).

wavelengths are  $O(1)$  over the values of  $B$  for which there is an AI, then these destabilizing AIs would be expected to persist and not be quickly saturated by nonlinear effects. Hence it is possible to tune the parameters of the compliant walls to induce an AI, in a seemingly unbounded domain, where there is no AI in the true unbounded, or rigid wall cases, if this is beneficial.

In Figs. 10 and 14 we considered the effect of compliant walls on the AI for a fixed shear value  $\Lambda$ . However, for a fixed wall, we can calculate the regions of AI, as was done for a rigid wall in Fig. 6. This is done for a wall with  $(B, K, m) = (2, 10, 0.1)$  in Fig. 16 for (a) varicose and (b) sinuous modes. The gray region again indicates a region of AI. These results show that compliant walls are able to expand the region of AI to much lower values of shear  $\Lambda$  than the rigid wall case (dashed lines), i.e., we are able to observe an AI where in the rigid wall limit we only see CI. This is primarily a result of the the wall-induced modes becoming unstable for lower shear values. For the varicose case, it is clear that we see the largest increase in the AI region around  $h \approx 1$ , while for sinuous modes the largest increase is at strong confinement, or small  $h$ .

The piecewise linear flow we have considered in this section is not a true reflection of what we expect in reality, but Ref. [3] showed that models such as these can qualitatively predict stability results for smooth flows. In the results we present in Sec. IV B, some of the induced growth rates are small, and so in the next section we examine how these results are modified when a smooth base flow is considered.

### C. Smooth base flow profile

In this section we consider a smooth version of the base flow (1) in order to, first, show that the effects seen in Sec. IV A and Sec. IV B are not artifacts of the piecewise linear setup and, second, to show how the smooth nature of the base flow affects these results. In reality, our base flow would be smooth, even if sharp changes in velocity occur, hence we can consider this as a more “realistic” profile.

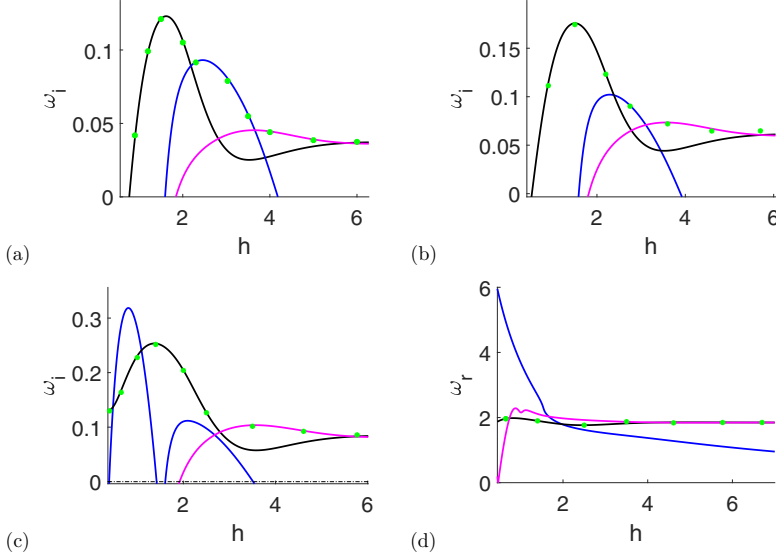


FIG. 13. Varicose mode: Plots of AI growth rate  $\omega_i$  as a function of confinement  $h$  as we vary shear layer thickness (a)  $\delta = 0.5$ , (b)  $\delta = 0.35$ , and (c)  $\delta = 0.15$ , where the dots represent  $\omega_i^{\text{num}}$  values. The other flow parameters are as in Fig. 11(a) with  $B = 2$ . In panel (d) we plot  $\omega_r$  for the case  $\delta = 0.15$ , corresponding to panel (c).

To smooth the profile we consider the function  $dU/dz$  from (1), which will be piecewise constant, and replace the step functions with hyperbolic tangents with some smoothing parameter  $\Delta$  [24,25]. These functions are then integrated with respect to  $z$  to give the smooth expression for  $U(z)$  as

$$U(z) = U_2 + (U_1 - U_2) \left[ \frac{1}{2} + \frac{\Delta}{2\delta} \log \left\{ \frac{\cosh\left(\frac{z-h_1-\delta}{\Delta}\right)}{\cosh\left(\frac{z-h_1}{\Delta}\right)} \right\} \right],$$

which in nondimensional form is

$$U^*(z^*) = (1 - \Lambda) + \Lambda \left[ 1 + \frac{\Delta^*}{\delta^*} \log \left\{ \frac{\cosh\left(\frac{z^*-1-\delta^*}{\Delta^*}\right)}{\cosh\left(\frac{z^*-1}{\Delta^*}\right)} \right\} \right]. \quad (35)$$

Here the stars denote dimensionless quantities, and, as before, we now neglect the stars in what follows. A plot of this base flow profile for a range of smoothing parameters  $\Delta$  is given in Fig. 17. Note that in the limit as  $\Delta \rightarrow 0$ , (35) tends to the original piecewise linear base flow in (1), hence the expectation is we should be able to compare the smooth and piecewise linear results in this limit. One consequence of using a smooth base flow is that we are no longer able to derive an analytic dispersion relation, and this must now be done numerically. This is achieved using a shooting method, numerically integrating the Rayleigh equation (13), from  $z = 0$  to the unperturbed upper wall position at  $z = 1 + h + \delta$  via the fourth-order Runge-Kutta method, with boundary conditions  $w(0) = 0$  and  $Dw(0) = 1$ . The value of  $\omega$  is then updated such that the boundary condition  $\alpha^2 Qw(1 + h + \delta) - [\alpha U(1 + h + \delta) - \omega]^2 Dw(1 + h + \delta) = 0$  via Newton iterations. In Fig. 18, we plot the effects of varying  $\Delta$  on the AI growth rates for the varicose mode from Fig. 13 for a range of  $\delta$  values. The equivalent results for the piecewise linear results are in Fig. 13(a) for  $\delta = 0.5$  and Fig. 13(c) for  $\delta = 0.15$ . When we compare the  $\Delta = 0.025$  results in Figs. 18(a) and 18(c) with these equivalent piecewise linear results we find them to be almost identical, with the shear-induced mode (blue curve) significant for  $\delta = 0.5$  [Fig. 18(a)], but no longer a pinch point for  $\delta = 0.15$  [Fig. 18(b)]. This is again confirmed by the values of  $\omega^{\text{num}}$ . Hence, it is the case that in a

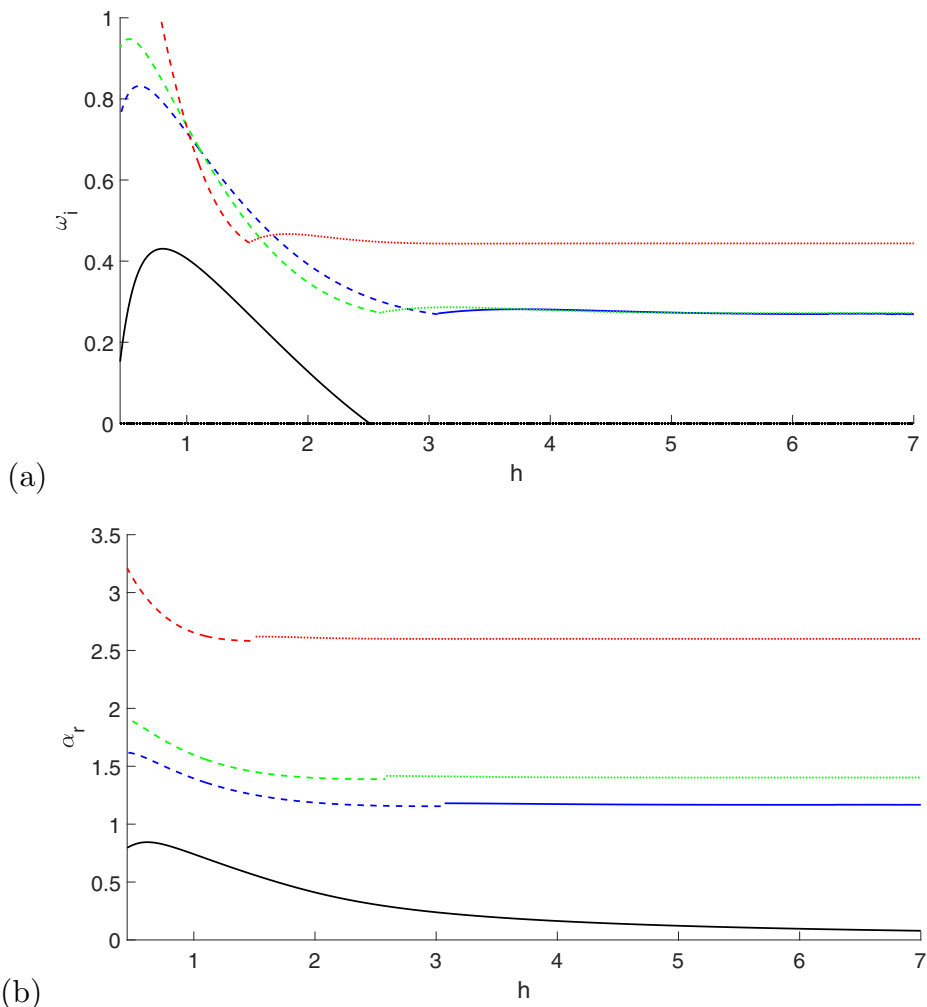


FIG. 14. Plot of (a) the dominant growth rates  $\omega_i$  and (b) the corresponding values of  $\alpha_r$ , for three relevant saddle points for the sinuous mode, as a function of the confinement parameter  $h$ . The fixed parameters are  $\Lambda = -1$  with wall parameters  $(K, m, d, T) = (10, 0.1, 0, 0)$  and  $B = 0.1$  (red line),  $B = 1$  (green lines), and  $B = 2$  (blue lines). The rigid wall limit result is given by the black line. The solid line give the  $SI_1$  saddle growth rates, the dashed lines give the  $WI_1$  saddle growth rate and the dotted line represents the  $WI_2$  wall mode.

true smooth flow, we expect the introduction of bounding compliant walls to lead to an AI at large values of the parameter  $h$  that is not present for rigid walls.

As we increase the profile smoothness we observe an overall reduction in the AI growth rate of the flow, but the AI growth rate for the shear-induced mode is less affected than the other two modes. As a result, this shear-induced mode begins to play a more significant role to the AI of the flow as  $\Delta$  is increased.

Overall, this analysis shows that the piecewise linear analysis from previous section does indeed capture the significant AI features of the jet or wake flow when bounded by compliant walls.

## V. EFFECT OF VISCOSITY

In the work presented in the previous sections we have neglected the effect of viscosity, in particular the effect on the flow due to the existence of viscous boundary layers at the wall.

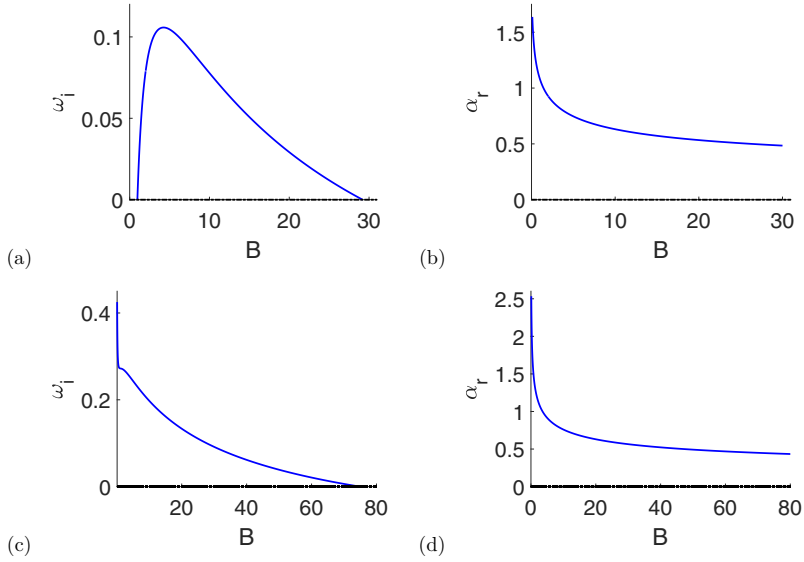


FIG. 15. Plot of  $(\omega_i, \alpha_r)$  in the  $h \rightarrow \infty$  limit for [(a) and (b)] the varicose mode in Fig. 11 and [(c) and (d)] the sinuous mode in Fig. 14 as a function of  $B$ .

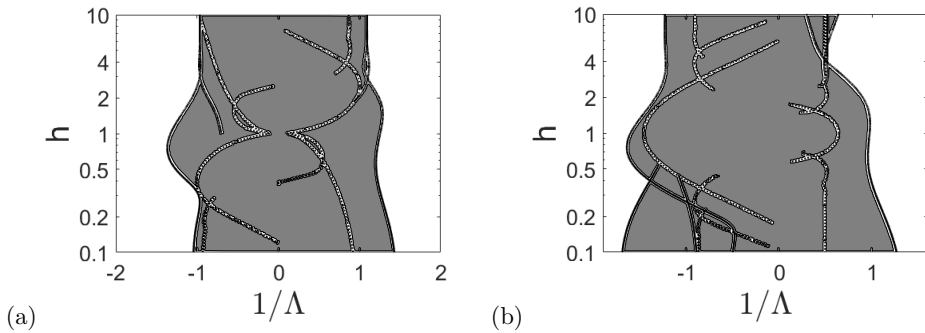


FIG. 16. Regions of AI for (a) varicose and (b) sinuous modes, when the flow is confined by compliant walls with  $(B, K, m) = (2, 10, 0.1)$  and  $d = T = 0$ . Gray regions indicate AI while white regions depict CI. Dotted lines indicate AI-CI boundaries found from the rigid wall case, while solid lines represent the AI-CI boundaries of the compliant wall case.

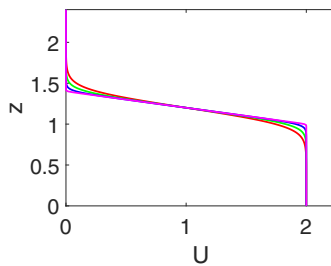


FIG. 17. A plot of the smooth base flow (35) for  $(\Lambda, \delta, h) = (1, 0.4, 1)$  with  $\Delta = 0.15$  (red line),  $\Delta = 0.1$  (green line),  $\Delta = 0.05$  (blue line), and  $\Delta = 0.01$  (magenta line).

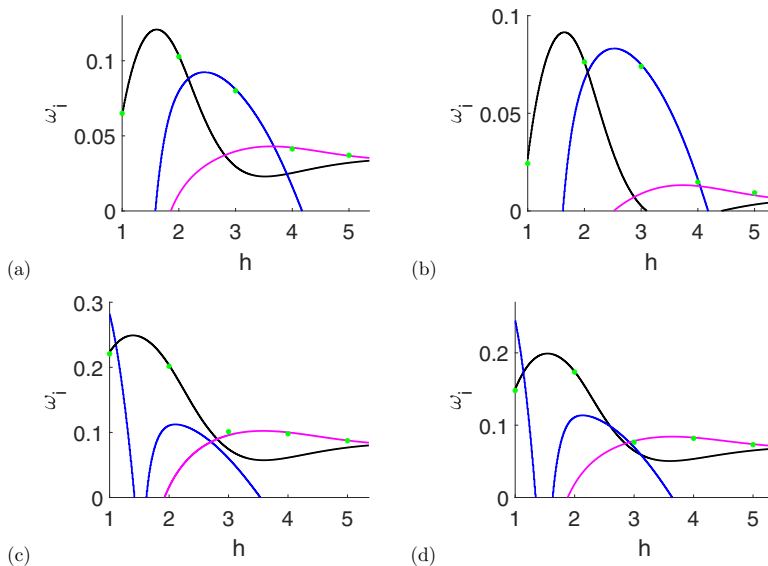


FIG. 18. Plot of  $\omega_i$  for the dominate saddles for varicose modes using the smooth profile with  $(\Lambda, h) = (1, 1)$  and wall parameters  $(B, K, T, m, d) = (2, 10, 0, 0.1, 0)$  with (a)  $(\delta, \Delta) = (0.5, 0.025)$ , (b)  $(\delta, \Delta) = (0.5, 0.1)$ , (c)  $(\delta, \Delta) = (0.15, 0.025)$ , and (d)  $(\delta, \Delta) = (0.15, 0.1)$ . The dots represent  $\omega_i^{\text{num}}$  values, and the piecewise linear equivalent results are in Figs. 13(a) and 13(c), respectively.

Juniper *et al.* [26] considered the effect of these boundary layers on a two-dimensional wake flow at intermediate Reynolds number of  $\text{Re} = 100$ . What they found at strong confinement values ( $h \leq 1.5$ ) was that the apparent instability identified by the inviscid analysis was actually stabilized. This was due in no small part to the fact that the boundary layers became close to the shear layers, plus the wake recirculation region was increased. However, for weak confinement, the viscous and inviscid conclusions agree qualitatively, i.e., the AI persists, albeit with a reduced growth rate for the viscous result. The same conclusion was drawn for wakes with coflow, similar to those considered here [27].

The implication of these results on the results presented in this paper, in particular those presented in Fig. 16, is that for strongly confined flows we cannot guarantee that the significant increase in the AI growth rate we find in the presence of the compliant wall is enough to overcome the stabilizing factors of viscosity for moderate Reynolds numbers. It is likely this will have an effect, but this is left to a future study. However, for weakly confined jets and wakes, we can expect the extended region of AI observed in this inviscid study to persist and be significant to these types of flow.

## VI. DISCUSSION AND CONCLUSION

In this work we examined the effects of having two identical bounding compliant walls on the AI/CI characteristics of inviscid jet and wake flows for various shear and confinement ratios. The AI analysis used locates the modes of zero group velocity by numerically solving the dispersion relation for the instability using Newton iterations and allowed us to track these modes as the compliant wall parameters were varied. This was carried out for both a piecewise linear and a smooth base flow profile, both of which showed qualitatively similar results, with the smoothed function typically damping the growth rates compared to the piecewise linear profile.

We have shown that the addition of compliant walls leads to new saddle points being generated in the complex wave-number plane, as well as modifying the saddles which exist in the rigid wall limit. The new saddles traverse the complex plane as the wall parameters are varied and it becomes

ambiguous as to which saddle points are pinch points and contribute to the AI of the flow. This ambiguity was overcome in this paper by numerically evaluating the Fourier inversion integral (31) via arbitrary precision calculations to identify which saddle dominates the AI properties of the flow.

It was shown that the addition of compliant walls leads to a mechanism which can control the existing flow instabilities, either enhancing or diminishing them. The walls can also induce their own disturbances, i.e., wall-induced modes, as well as modifying the existing shear-induced modes, which exist in the rigid wall limit. The effectiveness of the walls at (de)stabilizing the flow depends heavily on the flow itself, as well as its stability characteristics behavior at small and large values of the wall parameters.

In the majority of cases considered here for realistic wall parameters, in the absence of wall damping  $d$ , we find that compliant walls appear to make the overall flow-wall system more unstable than in the rigid wall limit and increase the range of  $\Lambda$  and  $h$  for which we see AI. We also find that the compliant walls induce an AI which persists for large values of the confinement parameter,  $h$ , i.e., as the walls move apart, the AI persists even in the limit  $h \rightarrow \infty$ . This phenomena is seen for both varicose and sinuous modes and is due to the existence of wall-induced modes. In nearly all cases we find that adding a damping fluid substrate to the wall construction acts to remove any AI, as expected, except in those flow and wall parameter cases where the rigid wall limit has an AI, while intermediate wall values does not. In this case increased damping enhances the AI. Overall, obtaining a balance between the stability of the shear-induced modes and the stability of the wall-induced modes is challenging, as stabilizing the shear-induced modes, in the absence of wall damping, usually leads to an AI in the wall-induced modes and vice versa.

In the case of smooth velocity profiles, we find qualitatively similar instability behavior as for the piecewise linear velocity profile. At small smoothness values,  $\Delta$ , it was shown that the AI behavior for both sinuous and varicose modes behaves identically to the piecewise linear case. As  $\Delta$  increases, the growth rates of the wall-induced modes reduce in magnitude more quickly than the shear-induced modes, and hence in smooth flows the wall-induced modes are less significant to the overall flow stability than in the piecewise linear flows. However, the piecewise linear approximation gives an excellent qualitative description of the overall flow stability properties and thus has a significant contribution to make to flows with compliant walls.

We note that the removal of viscosity has a significant effect on the flows instability, in the sense that we neglect the viscous boundary layers at the wall. In the literature, these layers have been shown to have a stabilizing effect on the flow bound by rigid walls at strong confinement but has little influence on the flow's stability at weak confinement. Therefore, we highlight that at strong confinement, we expect to see a stronger damping effect in our results if we were to include viscosity. At weaker confinement, on the other hand, we expect qualitatively similar results to those found in this paper.

#### ACKNOWLEDGMENTS

R.P. thanks the EPSRC for funding his Ph.D. studentship under Grant No. EP/V520111/1 and M.R.T. is supported by the EPSRC under Grant No. EP/W006545/1. For the purpose of open access, the authors have applied a Creative Commons Attribution (CC BY) licence to any Author Accepted Manuscript version arising.

#### APPENDIX: DERIVATIVES OF THE DISPERSION RELATION (24)

To numerically calculate the values of  $\alpha$  and  $\omega$  signifying an absolute instability, we use Newton iterations to solve  $\mathbb{D}(\alpha, \omega) = \mathbb{D}_\alpha(\alpha, \omega) = 0$  simultaneously, where the subscript denotes a partial derivative. Newton's method gives the update for the values  $(\alpha, \omega)^T$  via

$$\begin{pmatrix} \alpha^{n+1} \\ \omega^{n+1} \end{pmatrix} = \begin{pmatrix} \alpha^n \\ \omega^n \end{pmatrix} - \begin{bmatrix} \mathbb{D}_\alpha(\alpha^n, \omega^n) & \mathbb{D}_\omega(\alpha^n, \omega^n) \\ \mathbb{D}_{\alpha\alpha}(\alpha^n, \omega^n) & \mathbb{D}_{\alpha\omega}(\alpha^n, \omega^n) \end{bmatrix}^{-1} \begin{pmatrix} \mathbb{D}(\alpha^n, \omega^n) \\ \mathbb{D}_\alpha(\alpha^n, \omega^n) \end{pmatrix},$$

where  $n$  denotes the iteration number. For the compliant wall dispersion relation in (24) these components are

$$\begin{aligned}\mathbb{D}_\alpha^{v*} &= \left(Q + \alpha \frac{\partial Q}{\partial \alpha}\right) X^v + \alpha Q \frac{\partial X^v}{\partial \alpha} + 2(1 - \Lambda)(\alpha(1 - \Lambda) - \omega) Y^v + (\alpha(1 - \Lambda) - \omega)^2 \frac{\partial Y^v}{\partial \alpha}, \\ \mathbb{D}_\omega^{v*} &= \alpha \frac{\partial Q}{\partial \omega} X^v + \alpha Q \frac{\partial X^v}{\partial \omega} - 2\omega(\alpha(1 - \Lambda) - \omega) Y^v + (\alpha(1 - \Lambda) - \omega)^2 \frac{\partial Y^v}{\partial \omega},\end{aligned}$$

and

$$\begin{aligned}\mathbb{D}_{\alpha\alpha}^{v*} &= \left(2 \frac{\partial Q}{\partial \alpha} + \alpha \frac{\partial^2 Q}{\partial \alpha^2}\right) X^v + 2 \left(Q + \alpha \frac{\partial Q}{\partial \alpha}\right) \frac{\partial X^v}{\partial \alpha} + \alpha Q \frac{\partial^2 X^v}{\partial \alpha^2} + 2(1 - \Lambda)^2 Y^v \\ &\quad + 4(1 - \Lambda)[\alpha(1 - \Lambda) - \omega] \frac{\partial Y^v}{\partial \alpha} + [\alpha(1 - \Lambda) - \omega]^2 \frac{\partial^2 Y^v}{\partial \alpha^2} \\ \mathbb{D}_{\alpha\omega}^{v*} &= \frac{\partial Q}{\partial \omega} X^v + \left(Q + \alpha \frac{\partial Q}{\partial \alpha}\right) \frac{\partial X^v}{\partial \omega} + \alpha \frac{\partial Q}{\partial \omega} \frac{\partial X^v}{\partial \alpha} + \alpha Q \frac{\partial^2 X^v}{\partial \alpha \partial \omega} - 2(1 - \Lambda) Y^v \\ &\quad + 2(1 - \Lambda)[\alpha(1 - \Lambda) - \omega] \frac{\partial Y^v}{\partial \omega} - 2\omega[\alpha(1 - \Lambda) - \omega] \frac{\partial Y^v}{\partial \alpha} + [\alpha(1 - \Lambda) - \omega]^2 \frac{\partial^2 Y^v}{\partial \alpha \partial \omega},\end{aligned}$$

where

$$X^v = -e^{-2\alpha h} D_+^{v*} + D_-^{v*}, \quad Y^v = -e^{-2\alpha h} D_+^{v*} - D_-^{v*},$$

for finite  $\delta$  and are given by (28) in the limit  $\delta \rightarrow 0$ . In this  $\delta \rightarrow 0$  limit then we find for varicose modes

$$\begin{aligned}\frac{\partial X^v}{\partial \alpha} &= [\alpha(1 - \Lambda) - \omega] \{2(1 - \Lambda) \coth(\alpha h) - [\alpha(1 - \Lambda) - \omega] h \operatorname{csch}^2(\alpha h)\}, \\ &\quad + [\alpha(1 + \Lambda) - \omega] \{2(1 + \Lambda) \coth(\alpha h) - [\alpha(1 + \Lambda) - \omega] \operatorname{csch}^2(\alpha)\} \\ \frac{\partial Y^v}{\partial \alpha} &= 2(1 - \Lambda)[\alpha(1 - \Lambda) - \omega] + 2(1 + \Lambda)[\alpha(1 + \Lambda) - \omega] \coth(\alpha) \coth(\alpha h) \\ &\quad - [\alpha(1 + \Lambda) - \omega]^2 [\operatorname{csch}^2(\alpha) \coth(\alpha h) + h \coth(\alpha) \operatorname{csch}^2(\alpha h)], \\ \frac{\partial X^v}{\partial \omega} &= -2[\alpha(1 - \Lambda) - \omega] \coth(\alpha h) - 2[\alpha(1 + \Lambda) - \omega] \coth(\alpha), \\ \frac{\partial Y^v}{\partial \omega} &= -2[\alpha(1 - \Lambda) - \omega] - 2[\alpha(1 + \Lambda) - \omega] \coth(\alpha) \coth(\alpha h), \\ \frac{\partial^2 X^v}{\partial \alpha^2} &= 2(1 - \Lambda)^2 \coth(\alpha h) - 4h(1 - \Lambda)[\alpha(1 - \Lambda) - \omega] \operatorname{csch}^2(\alpha h) \\ &\quad + 2h^2[\alpha(1 - \Lambda) - \omega]^2 \operatorname{csch}^2(\alpha h) \coth(\alpha h), \\ &\quad + 2(1 + \Lambda)^2 \coth(\alpha) - 4(1 + \Lambda)[\alpha(1 + \Lambda) - \omega] \operatorname{csch}^2(\alpha) \\ &\quad + 2[\alpha(1 + \Lambda) - \omega]^2 \operatorname{csch}^2(\alpha) \coth(\alpha), \\ \frac{\partial^2 Y^v}{\partial \alpha^2} &= 2(1 - \Lambda)^2 + (1 + \Lambda)^2 \coth(\alpha) \coth(\alpha h) \\ &\quad - 4(1 + \Lambda)[\alpha(1 + \Lambda) - \omega] [\operatorname{csch}^2(\alpha) \coth(\alpha h) + h \coth(\alpha) \operatorname{csch}^2(\alpha h)] \\ &\quad + 2(\alpha(1 + \Lambda) - \omega)^2 [\coth(\alpha) \operatorname{csch}^2(\alpha) \coth(\alpha h) + h \operatorname{csch}^2(\alpha) \operatorname{csch}(\alpha h) \\ &\quad + h^2 \coth(\alpha) \operatorname{csch}^2(\alpha h) \coth(\alpha h)],\end{aligned}$$



$$\begin{aligned} \frac{\partial^2 X^v}{\partial \alpha \partial \omega} &= -2(1 - \Lambda) \coth(\alpha h) + 2h[\alpha(1 - \Lambda) - \omega] \operatorname{csch}^2(\alpha h) \\ &\quad - 2(1 + \Lambda) \coth(\alpha) + 2[\alpha(1 + \Lambda) - \omega] \operatorname{csch}^2(\alpha), \\ \frac{\partial^2 Y^v}{\partial \alpha \partial \omega} &= -2(1 - \Lambda) - 2(1 + \Lambda) \coth(\alpha) \coth(\alpha h) \\ &\quad + 2[\alpha(1 + \Lambda) - \omega][\operatorname{csch}^2(\alpha) \coth(\alpha h) + h \coth(\alpha) \operatorname{csch}^2(\alpha h)], \end{aligned}$$

and

$$\begin{aligned} \frac{\partial Q}{\partial \alpha} &= 4B\alpha^3 + 2T\alpha, & \frac{\partial Q}{\partial \omega} &= -2m\omega - id, \\ \frac{\partial^2 Q}{\partial \alpha^2} &= 12B\alpha^2 + 2T, & \frac{\partial^2 Q}{\partial \alpha \partial \omega} &= 0. \end{aligned}$$


---

- [1] P. Huerre and P. A. Monkewitz, Local and global instabilities in spatially developing flows, *Annu. Rev. Fluid Mech.* **22**, 473 (1990).
- [2] L. Weilgart, The impact of ocean noise pollution on fish and invertebrates, Report for OceanCare, Switzerland (2018).
- [3] M.-H. Yu and P. A. Monkewitz, The effect of nonuniform density on the absolute instability of two-dimensional inertial jets and wakes, *Phys. Fluids* **2**, 1175 (1990).
- [4] M. P. Juniper and S. M. Candel, The stability of ducted compound flows and consequences for the geometry of coaxial injectors, *J. Fluid Mech.* **482**, 257 (2003).
- [5] M. P. Juniper, The effect of confinement on the stability of two-dimensional shear flows, *J. Fluid Mech.* **565**, 171 (2006).
- [6] M. P. Juniper, The full impulse response of two-dimensional jet/wake flows and implications for confinement, *J. Fluid Mech.* **590**, 163 (2007).
- [7] J. Healey, A new Type of convective instability with exponential growth perpendicular to the basic flow, *J. Fluid Mech.* **560**, 279 (2006).
- [8] M. P. Juniper, The effect of confinement on the stability of non-swirling round jet/wake flows, *J. Fluid Mech.* **605**, 227 (2008).
- [9] M. O. Kramer, Boundary-layer stabilization by distributed damping, *J. Aerosp. Sci.* **27**, 69 (1960).
- [10] T. B. Benjamin, Effects of a flexible boundary on hydrodynamic stability, *J. Fluid Mech.* **9**, 513 (1960).
- [11] T. B. Benjamin, The threefold classification of unstable disturbances in flexible surfaces bounding inviscid flows, *J. Fluid Mech.* **16**, 436 (1963).
- [12] P. Carpenter and A. Garrad, The hydrodynamic stability of flow over Kramer-type compliant surfaces. Part 1. Tollmien-Schlichting instabilities, *J. Fluid Mech.* **155**, 465 (1985).
- [13] P. Carpenter and A. Garrad, The hydrodynamic stability of flow over Kramer-type compliant surfaces. part 2. Flow-induced surface instabilities, *J. Fluid Mech.* **170**, 199 (1986).
- [14] P. W. Carpenter, C. Davies, and A. D. Lucey, Hydrodynamics and compliant walls: Does the dolphin have a secret? *Curr. Sci.* **79**, 758 (2000).
- [15] M. T. Landahl, On the stability of a laminar incompressible boundary layer over a flexible surface, *J. Fluid Mech.* **13**, 609 (1962).
- [16] P. G. Drazin, *Introduction to Hydrodynamic Stability*, Vol. 32 (Cambridge University Press, Cambridge, UK, 2002).
- [17] E. J. Brambley, Fundamental problems with the model of uniform flow over acoustic linings, *J. Sound Vib.* **322**, 1026 (2009).
- [18] P. G. Drazin and W. H. Reid, *Hydrodynamic Stability* (Cambridge University Press, Cambridge, UK, 2004).

- [19] P. Huerre, Open shear flow instabilities, in *Perspective in Fluid Dynamics: A Collective Introduction to Current Research*, edited by G. K. Batchelor, H. K. Moffatt, and M. G. Worster (Cambridge University Press, Cambridge, UK, 2000).
- [20] P. J. Schmid, D. S. Henningson, and D. Jankowski, Stability and transition in shear flows, *Appl. Mech. Rev.* **55**, B57 (2002).
- [21] R. J. Briggs, *Electron-stream Interaction with Plasmas* (MIT press, Cambridge, MA, 1964), Vol. 187.
- [22] D. M. Smith, Algorithm 693: A FORTRAN package for floating-point multiple-precision arithmetic, *ACM Trans. Math. Softw.* **17**, 273 (1991).
- [23] S. Rees and M. Juniper, The effect of confinement on the stability of viscous planar jets and wakes, *J. Fluid Mech.* **656**, 309 (2010).
- [24] J. Healey, Destabilizing effects of confinement on homogeneous mixing layers, *J. Fluid Mech.* **623**, 241 (2009).
- [25] M. Turner, J. Healey, S. Sazhin, and R. Piazzesi, Wave packet analysis and break-up length calculations for an accelerating planar liquid jet, *Fluid Dyn. Res.* **44**, 015503 (2012).
- [26] M. Juniper, O. Tammisola, and F. Lundell, The local and global stability of confined planar wakes at intermediate reynolds number, *J. Fluid Mech.* **686**, 218 (2011).
- [27] O. Tammisola, F. Lundell, P. Schlatter, A. Wehrfritz, and L. D. Söderberg, Global linear and nonlinear stability of viscous confined plane wakes with co-flow, *J. Fluid Mech.* **675**, 397 (2011).